



Space Environment Effects: Low-Altitude Trapped Radiation Model

S.L. Huston and K.A. Pfitzer

The Boeing Company, Huntington Beach, California

Prepared for Marshall Space Flight Center
under Contract NAS8-40295
and sponsored by
the Space Environments and Effects Program
managed at the Marshall Space Flight Center

National Aeronautics and
Space Administration

Marshall Space Flight Center • MSFC, Alabama 35812

Available from:

NASA Center for AeroSpace Information
800 Elkridge Landing Road
Linthicum Heights, MD 21090-2934
(301) 621-0390

National Technical Information Service
5285 Port Royal Road
Springfield, VA 22161
(703) 487-4650

CONTENTS

CONTENTS	iii
LIST OF FIGURES	v
1. INTRODUCTION.....	1-1
1.1 BACKGROUND AND OVERVIEW	1-1
1.2 SUMMARY	1-2
2. DATA SOURCE.....	2-1
2.1 SPACECRAFT	2-1
2.2 ORBITAL COVERAGE	2-2
2.3 DETECTORS	2-2
2.3.1 Particle Telescopes	2-3
2.3.2 Omnidirectional Detectors.....	2-4
2.4 INSTRUMENT ANALYSIS	2-6
2.4.1 Detector Threshold and Particle Discrimination.....	2-6
2.4.2 Secondary Production.....	2-7
2.4.3 Energy Cutoffs	2-7
2.4.4 Geometric Factor.....	2-8
2.4.5 Detector Efficiency.....	2-11
2.4.6 Data Quantization.....	2-11
2.4.7 Summary of Instrument Analysis.....	2-11
2.5 DATA ARCHIVE	2-11
3. DATA PROCESSING.....	3-1
3.1 GENERATION OF CORRECTED DATA FILES	3-1
3.1.1 Read Logical Record	3-1
3.1.2 Data Summing.....	3-1
3.1.3 Compute New Position and Magnetic Field Parameters.....	3-2
3.1.4 Create New Archive File.....	3-3
3.2 TIME SHIFT.....	3-3
3.3 DETECTOR BACKGROUNDS	3-4
3.4 DATA GRID.....	3-4
3.5 DATA SMOOTHING	3-5
4. DATA ANALYSIS	4-1
4.1 TEMPORAL VARIATIONS.....	4-1
4.2 VARIATIONS WITH SOLAR ACTIVITY.....	4-2
4.3 SOLAR PARTICLE EVENTS	4-4

4.4	PITCH ANGLE DISTRIBUTIONS	4-4
4.5	INTERCOMPARISON OF SPACECRAFT	4-5
4.6	COMPARISON WITH AP8	4-5
4.7	NOAA-10 DATA ANOMALY	4-6
5.	MODEL DEVELOPMENT.....	5-1
5.1	DETERMINATION OF MODEL PARAMETERS	5-1
5.2	MODEL IMPLEMENTATION	5-3
5.3	MODEL RESULTS	5-5
5.4	NOAA-10 P7 CHANNEL	5-7
5.5	COMPARISON WITH AP8	5-8
6.	SUMMARY AND CONCLUSIONS.....	6-1
6.1	NOAAPRO MODEL	6-1
6.2	MEPED DATA BASE	6-1
6.3	FUTURE EFFORTS	6-2
7.	REFERENCES	7-1
APPENDIX A: TIROS/NOAA DATA SET		A-1
APPENDIX B: NOAAPRO MODEL.....		B-1
APPENDIX C: CORRECTED MEPED DATA BASE		C-1

LIST OF FIGURES

Figure 2-1. Temporal coverage of the MEPED instrument on the TIROS/NOAA spacecraft. The dashed line shows the solar 10.7 cm radio flux ($F_{10.7}$), and the triangles indicate data points used for this study.....	2-2
Figure 2-2. SEM instruments on the TIROS/NOAA spacecraft.....	2-3
Figure 2-3. Spacecraft coverage in B/B_{min} -L space used in the present study.	2-3
Figure 2-4. Proton energy spectra from AP8 MIN and MAX, showing the coverage of the MEPED omnidirectional detectors.	2-6
Figure 2-5. Plot of ΔE vs. E for the MEPED omnidirectional detectors.....	2-7
Figure 3-1. Example of data using B, L coordinates from NOAA archive file.....	3-2
Figure 3-2. Same data as Figure 3-1, but organized using new B, L procedure.	3-3
Figure 3-3. (a) Count rate as a function of L for $B/B_{min}=1.0$, with no time shift introduced. Note the bifurcation in the data. (b) Same data with a time shift of -16 seconds applied.	3-4
Figure 3-4. Average background count rate in counts per 8 second interval for the period 1978 – 1995.	3-5
Figure 3-5. Model grid in ζ -L' space. The points indicate where MEPED data are available.	3-5
Figure 3-6. Model grid in B/B_{min} -L space.....	3-5
Figure 4-1. Temporal variation of the >80 MeV proton flux for several values of L at the geomagnetic equator ($B/B_{min}=1.0$). The dashed curve shows the solar $F_{10.7}$ flux for the same period.	4-2
Figure 4-2. Temporal variation of the >80 MeV proton flux for several values of L at $B/B_{min}=2.0$	4-2
Figure 4-3. Variation of the >80 MeV proton flux with solar activity for several values of L at $B/B_{min}=2.0$	4-3
Figure 4-4. Variation of the >80 MeV proton flux with solar activity for several values of L at the geomagnetic equator ($B/B_{min}=1.0$).	4-3
Figure 4-5. Omnidirectional count rate as a function of B/B_{min} at $L=1.2$ for solar minimum and solar maximum conditions.	4-5
Figure 4-6. Pitch angle distributions for $L=1.2$ at solar minimum and solar maximum determined using the omnidirectional flux distributions shown in the previous figure.	4-5
Figure 4-7. Comparison of P8 count rates measured by TIROS-N and NOAA-6 at the geomagnetic equator in March 1980.	4-6
Figure 4-8. Comparison of P8 count rates measured by NOAA-6 and NOAA-10 at the geomagnetic equator in March 1980.	4-6
Figure 4-9. Comparison of P8 count rates measured by NOAA-10 and NOAA-12 at the geomagnetic equator in March 1980.	4-6
Figure 4-10. Comparison of P8 count rates measured by NOAA-12 and NOAA-14 at the geomagnetic equator in March 1980.	4-6
Figure 4-11. Comparison of measured >80 MeV proton fluxes with AP8 predictions. a) Solar minimum. b) Solar maximum. Solid symbols show NOAA data; open symbols/lines show AP8 predictions.....	4-7
Figure 4-12. Count rates in the P6, P7, and P8 channels as a function of time. Note the sharp drop in the P7 count rate in 1986 and the sharp increase in 1991.	4-8
Figure 5-1. Variation of χ^2 , a_0 , and a_1 with assumed phase lag for a typical point in ζ -L' space.	5-2
Figure 5-2. Isocontours of phase lag in ζ -L' space for the P8 channel.....	5-3
Figure 5-3. Isocontours of a in ζ -L' space for the P8 channel.	5-3

Figure 5-4. Isocontours of a_1 in ζ - L' space for the P8 channel.....	5-4
Figure 5-5. Comparison of the P8 count rate predicted by the NOAAAPRO model with actual data at the geomagnetic equator ($\zeta=90^\circ$).	5-5
Figure 5-6. Comparison of the P6 count rate predicted by NOAAAPRO with measured data at $L'=0.10$	5-6
Figure 5-7. Comparison of the P7 count rate predicted by NOAAAPRO with measured data at $L'=0.10$	5-6
Figure 5-8. Comparison of the P8 count rate predicted by NOAAAPRO with measured data at $L'=0.10$	5-7
Figure 5-9. Scatter plot showing the P8 count rate predicted by NOAAAPRO vs. the actual measured count rate, for the entire data set used to develop the model. The gray diagonal line indicates a perfect correlation.	5-9
Figure 5-10. Probability of obtaining a given percent error using the NOAAAPRO model.	5-9
Figure 5-11. Ratio of fluence predicted by NOAAAPRO to that predicted by AP8 for circular polar orbits of various altitudes at solar minimum conditions.....	5-10
Figure 5-12. Ratio of fluence predicted by NOAAAPRO to that predicted by AP8 for circular polar orbits of various altitudes at solar maximum conditions.	5-10

1. INTRODUCTION

1.1 Background and Overview

Accurate models of the Earth's trapped energetic proton environment are required for both piloted and robotic space missions. For piloted missions, the concern is mainly total dose to the astronauts, particularly in long-duration missions and during extravehicular activity (EVA). As astronomical and remote sensing detectors become more sensitive, the proton flux can induce unwanted backgrounds in these instruments. Observing sessions on the Hubble Space Telescope, for example, are planned so that certain measurements are avoided during passes through the South Atlantic Anomaly (SAA). All spacecraft are potentially susceptible to single event effects (SEE), which affect electronic systems and can cause system failure. In the future, solar orbital transfer vehicles (SOTVs) may take months to spiral up to geosynchronous orbit, and solar cells will be subject to degradation from trapped particles.

Accurate flux predictions are required to predict dose rate and total dose, as well as SEE rates. Accuracy in the flux predictions in turn requires the ability to model the variations over the solar cycle. Geographic accuracy is required for scheduling EVAs and observing sessions.

Given these requirements for accuracy, the current U.S. model AP8 (Reference 1) is increasingly being recognized as inadequate. Although it contains separate models for solar minimum and maximum conditions, AP8 does not model the variation through the solar cycle. It also does not address the long-term variations due to the secular variation in the Earth's magnetic field (References 2 and 3). The model can be used to predict the average proton flux for a given orbit, but it cannot be used to predict the instantaneous flux along an orbit, and thus cannot be used for scheduling observing sessions or EVAs. Finally, recent studies (References 4, 5, and 6) have shown that AP8 does not accurately predict the actual flux.

Although AP8 has served its users well up until now, it is showing signs of age. AP8 was developed over 20 years ago using data primarily from the 1960s and early 1970s. Some of the drawbacks of AP8 include:

- No true solar cycle dependence. AP8 consists of models for solar maximum and solar minimum, but not in between. In addition, the solar maximum model was developed during a solar maximum period which was much smaller than more recent cycles.
- Does not account for the secular variation in the Earth's magnetic field. AP8 is tied to magnetic field models for the epochs during which it was developed. Thus it does not account for the reconfiguration of the trapped proton environment over time and cannot be used to predict the flux at a given position in geographic space.

- Although it extends to quite low altitudes, better resolution at low altitude is necessary for designers of new spacecraft which must operate for long periods of time at the lower edge of the inner zone.

1.2 Summary

Under NASA's Space Environment Effects (SEE) program, the Boeing Company has developed a new model for the low-altitude trapped proton environment. The model is based on nearly 20 years of data from the TIROS/NOAA weather satellites.

The model, which we have designated NOAAPRO (for NOAA protons), predicts the integral omnidirectional proton flux in three energy ranges: >16 , >36 , and >80 MeV. It contains a true solar cycle variation and accounts for the secular variation in the Earth's magnetic field. It also extends to lower values of the magnetic L parameter than does AP8. Thus, the model addresses the major shortcomings of AP8 discussed above.

For each energy channel, the model data are organized in terms of L and B/B_{\min} (although these parameters are mapped into coordinates more appropriate to the data space). The model consists of parameters which determine the absolute magnitude of the proton flux, the variation of the proton flux with the solar 10.7 cm radio flux ($F_{10.7}$), and the phase lag between $F_{10.7}$ and the proton flux. This approach results in a well-organized data set for two solar cycles, and can be extended into the future.

The model is provided as a user-callable FORTRAN subroutine which reads and interpolates a set of data files. The model is small and computationally efficient. It is also designed to be used with magnetic field models appropriate for the epoch for which predictions are desired.

The model reproduces the data set upon which it is based with excellent accuracy. Preliminary evaluations of the model (Reference 7) indicate that it correctly models the westward drift of the South Atlantic Anomaly, associated with the secular variation of the magnetic field. Comparisons with AP8 indicate that the new model predicts fluxes approximately twice as high as AP8.

The new model represents a major advancement in trapped radiation models. It is the first empirical model to include a true solar cycle dependence. It cannot be considered a true replacement for AP8, but it is an excellent beginning towards developing one.

In addition to the NOAAPRO model, we are also delivering the entire set of corrected MEPED data which we used to develop the model. This data set constitutes a rich resource for further studies, including trapped electrons and lower-energy protons. We have also supplied a routine for accessing the data base, which makes it useful to the entire community.

In Section 2 of this final report we discuss the source of the data used to develop the model, including a detailed discussion of the instruments and their calibration. Section 3 discusses the processing performed on the data to develop a data base from which the model could be developed. In Section 4 we discuss features of the data, including the variations of the proton flux with time and with solar activity. This analysis led to the selection of the model format. In Section 5, we discuss the development of the model itself, including determining the fitting parameters. We also discuss briefly how the model is implemented; more details of the model subroutines are given in Appendix B. In Section 5 we also compare the model to the data upon which it was based, and to AP8.

2. DATA SOURCE

Since 1978 the National Oceanic and Atmospheric Administration (NOAA) has operated a series of low-altitude, polar orbiting weather satellites designated TIROS/NOAA (Television and InfraRed Observation Satellite/National Oceanic and Atmospheric Administration). These satellites carry a Space Environment Monitor (SEM) package to detect and monitor the flux of ions and electrons at the satellite's orbit.

The SEM consists of three different instruments. The Medium Energy Proton and Electron Detector (MEPED) measures energetic electrons and protons mirroring above and precipitating into the high-latitude atmosphere. The Total Energy Detector (TED) measures the total energy flux carried into the atmosphere by particles of auroral energies. The High Energy Proton and Alpha Detector (HEPAD) measures protons and alpha particles, primarily of solar origin. (The HEPAD has not been flown on the TIROS/NOAA satellites since NOAA-7.) The data from the SEM are received in near-real time by NOAA and are archived on magnetic tape and CD-ROM.

Because essentially identical instruments have been flown for nearly twenty years, the data from the SEM provide an excellent data base for observing both the long- and short-term variations in the low-altitude trapped particle environment.

Information in this section comes primarily from References 8 through 10. Since we have used data only from the MEPED, this section concentrates on information required to understand the data from that instrument. In addition, to date we have only performed detailed analysis of the omnidirectional detectors, further restricting the discussion contained in this report. For more detailed descriptions of the other TIROS/NOAA instruments and MEPED data channels, the reader is referred to the original NOAA reports.

2.1 *Spacecraft*

Seven TIROS/NOAA spacecraft have been launched to date (April 1998). The lifetime of each satellite is nominally two years, and at most, two spacecraft are operating at any one time. Table 1 shows the periods when valid MEPED data are available from the different spacecraft, and Figure 2-1 shows the coverage graphically, compared with solar cycles 21 and 22. It can be seen that the TIROS/NOAA series cover nearly two full solar cycles. There are also several periods of overlap between two spacecraft, making it possible to evaluate the intercalibration between instruments on different spacecraft. These periods include the following:

- 1 July 1979 – 28 February 1981 (TIROS-N/NOAA-6)
- 11 October 1986 – 20 November 1986 (NOAA-6/NOAA-10)
- 1 June 1991 – 31 August 1991 (NOAA-10/NOAA-12)
- 29 December 1994 – present (NOAA-12/NOAA-14)

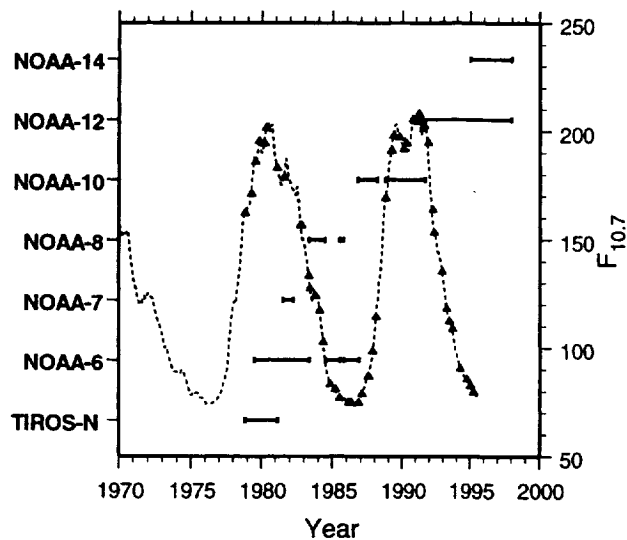


Figure 2-1. Temporal coverage of the MEPED instrument on the TIROS/NOAA spacecraft. The dashed line shows the solar 10.7 cm radio flux ($F_{10.7}$), and the triangles indicate data points used for this study.

850 km, 99° inclination orbits. Geographically, the satellites cover all longitudes and all latitudes from -81° to $+81^\circ$. Because of the Earth's dipole tilt, the satellites cover virtually all magnetic latitudes. Also because of the polar orbit, the satellites sample virtually all values of L , although the coverage in B , L space is somewhat limited. Figure 2-3 shows the region in B/B_{\min} , L space for which most of the analysis in this study was performed.

2.3 Detectors

The MEPED (Medium Energy Proton and Electron Detector) is that portion of the SEM designed

Figure 2-2 shows a sketch of the TIROS/NOAA spacecraft, including the instrument locations. The spacecraft velocity is in the $+y$ direction.

The satellites are placed in orbits of 850 km altitude and 99° inclination (nominally). The actual altitude varies between approximately 800 and 850 km, and the actual inclination varies between 98.5° and 99.0°.

2.2 Orbital Coverage

The SEM package was developed primarily to study phenomena in the auroral regions, a task made possible by the satellites' nominal

Table 1. Temporal coverage of MEPED data.

Spacecraft	MEPED Data Available
TIROS-N	2 November 1978 – 27 February 1981
NOAA-6	28 June 1979 – 9 May 1983 1 July 1984 – 30 June 1985 15 October 1985 – 18 November 1986
NOAA-7	11 July 1981 – 1 April 1982
NOAA-8	9 May 1983 – 14 June 1984 1 July 1985 – 14 October 1985
NOAA-10	11 October 1986 – 28 February 1988 1 October 1988 – 31 August 1991
NOAA-12	14 May 1991 –
NOAA-14	29 December 1994 –

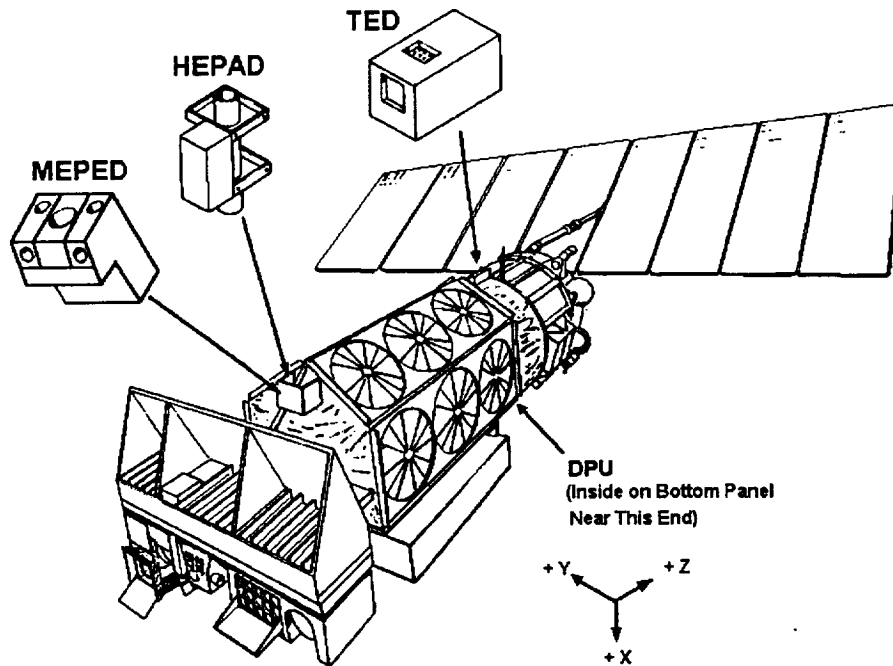


Figure 2-2. SEM instruments on the TIROS/NOAA spacecraft.

to measure the flux of protons (ions) and electrons mirroring above, and precipitating into, the high-latitude atmosphere. Each MEPED consists of two sensor assemblies: the directional (telescope) particle detectors and the omnidirectional proton detectors.

2.3.1 Particle Telescopes

The telescopes are mounted in two pairs, one of each pair detecting electrons, the other detecting protons (and heavier ions). One pair of detectors is mounted to view outward along the Earth-satellite radial vector zenith. At geomagnetic latitudes greater than 30 degrees, these detectors view charged particles that are in the atmospheric loss cone and will enter the atmosphere. The other detector pair is mounted to view at about 80 degrees to the first, and for magnetic latitudes greater than 30 degrees will measure particles that have pitch angles near 90 degrees (i.e., particles that are outside the loss cone and are trapped). For convenience these two detector telescopes are identified with the suffix 0 and 90. The local pitch angles of the particles observed by these two pairs of directional detectors at any point in the orbit are calculated using a

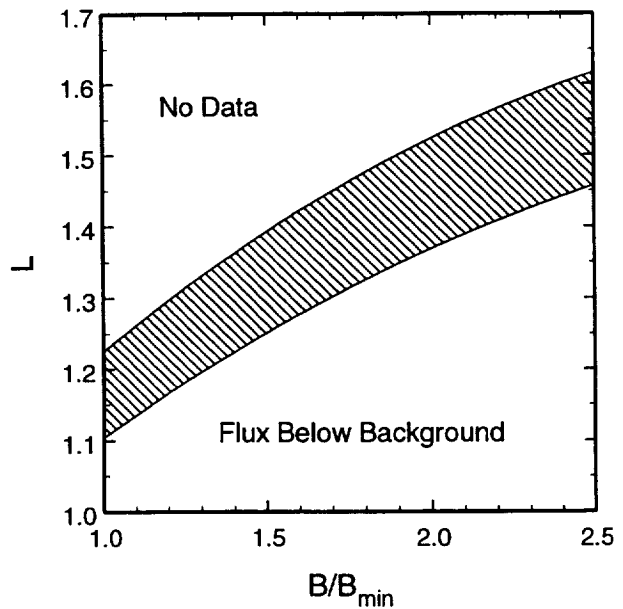


Figure 2-3. Spacecraft coverage in B/B_{min} , L space used in the present study.

model magnetic field developed at the National Space Science Data Center (Reference 11). The pitch angles are included in the archive tape record as part of the header information.

The electron detector is a thin (700 μm) 25 mm^2 solid-state detector covered by 0.51- μm -thick nickel foil (0.70 μm in the case of TIROS-N), that suppresses detector response to photons and reduces pulse pile-up caused by incident low-energy electrons or ions. Electronic pulse-height discrimination is used to select pulses due to incident electrons of nominal energies greater than 30 keV, 100 keV, and 300 keV (taking into account a nominal 5 keV energy loss as the electron passes through the foil). The contaminant response to protons that deposit more than 1 MeV in the detector is eliminated electronically. The detectors are, however, sensitive to protons between about 135 keV and 1 MeV. Data from the directional proton detectors may be used to correct for this effect.

The proton (ion) detector within each telescope pair is a two-element, solid-state detector telescope. The front element has an effective area of 25 mm^2 and thickness of 200 μm . The back element has an effective area of 50 mm^2 and a thickness of 200 μm . A 2500-gauss magnet is mounted across the input aperture of this detector assembly to prevent any electrons of energies less than 1.5 MeV from reaching the detectors. The front face of the front detector of the telescope is coated with an aluminum layer 18 $\mu\text{g cm}^{-2}$ thick, which serves both as an electrical contact and a suppresser of the detector's sensitivity to photons.

Electronic pulse height discrimination, together with coincidence logic on the pulses from the two detectors in the telescope, is used to select protons in four energy passbands (nominally 30–80 keV, 80–250 keV, 250–800 keV, and 800–2500 keV) and an integral channel for energies greater than 2.5 MeV. This detector is also sensitive to heavy ions (e.g. He and O) although the particle energies defining the passbands will be marginally higher than those given for protons. A second set of pulse logic isolates events due to ions ($Z \geq 2$) of energies between 6 and 55 MeV.

Table 2 lists the nominal energy ranges for the MEPED telescopes. The geometric factor for both the electron and proton directional detector systems is $9.5 \times 10^{-7} \text{ m}^2\text{-sr}$.

2.3.2 Omnidirectional Detectors

The omnidirectional sensors consist of three nominally identical Kevex Si(Li) solid-state detectors of 50 mm^2 area by 3 mm thickness (8 mm diameter, 0.69 g/cm^2 areal density), independently mounted under spherical shell moderators. The thickness (areal density) of each moderator determines the low-energy cutoff for that detector. Each detector has a full-opening view angle of 120 degrees in the zenith direction. The detectors are shielded from below by approximately 0.5 cm of Mallory, and the spacecraft itself provides additional shielding from below. Each detector has a full-opening viewing angle of 120° in the zenith direction. The detectors are advertised as having an upper energy threshold of approximately 215 MeV, determined from the requirement that a proton must lose at least 200 keV in passing through or being stopped by the detector. In reality, this threshold is set so low that, in effect, there is no

Table 2. MEPED particle telescope energy ranges

Data Channel	Energy Range
<i>Proton Telescopes</i>	
0I and 90I (ions, $Z \geq 2$)	6 – 55 MeV
0P1 and 90P1	30 – 80 keV
0P2 and 90P2	80 – 250 keV
0P3 and 90P3	250 – 800 keV
0P4 and 90P4	800 – 2500 keV
0P5 and 90P5	> 2500 keV
<i>Electron Telescopes</i>	
0E1 and 90 E1	> 30 keV
0E2 and 90E2	> 100 keV
0E3 and 90E3	> 300 keV

high-energy cutoff (see the next section for more details). The omnidirectional geometric factor (assuming an isotropic flux) is 0.215 cm^2 . Table 3 lists the characteristics of the MEPED omnidirectional sensors. Note that the moderator thicknesses listed in References 9 and 10 are incorrect; the thicknesses shown in our Table 3 have been verified by personal communication with Dr. David Evans, NOAA SEC (1997).

The equality of the secondary energy response of channels P6 and P7 is a reflection of the design decision to equalize the out-of-aperture response of the three omnidirectional sensors. Thus the P8 response can simply be subtracted from that of the P6 and P7 channels to obtain their respective primary responses of >16 and >36 MeV.

Figure 2-4 shows typical integral proton spectra from the NASA models AP8MAX and AP8MIN (Reference 1), along with arrows indicating the energy cutoffs of the three omnidirectional channels. These detectors have energy ranges at the ‘knee’ in the spectrum, making them ideal for model development. Any uncertainty in the energy thresholds of the instruments will have minimal effect on the accuracy of the fluxes measured.

Table 3. MEPED omnidirectional sensors.

Data Channel	Energy Response	Approx. Area, cm^2 (solid angle, sr)	Omnidirectional Geometric Factor	Moderator	
				Material	Thickness/ areal density
P6	16–80 MeV	0.5 (π)	$1.178 \text{ cm}^2\text{-sr}$	Aluminum	0.127 cm
	> 80 MeV	0.43 (4π)	$2.701 \text{ cm}^2\text{-sr}$		0.343 g/cm^2
P7	36–80 MeV	0.5 (π)	$1.178 \text{ cm}^2\text{-sr}$	Copper	0.218 cm
	> 80 MeV	0.43 (4π)	$2.701 \text{ cm}^2\text{-sr}$		1.94 g/cm^2
P8	> 80 MeV	0.43 (4π)	$2.701 \text{ cm}^2\text{-sr}$	Mallory	0.584 cm 11.5 g/cm^2

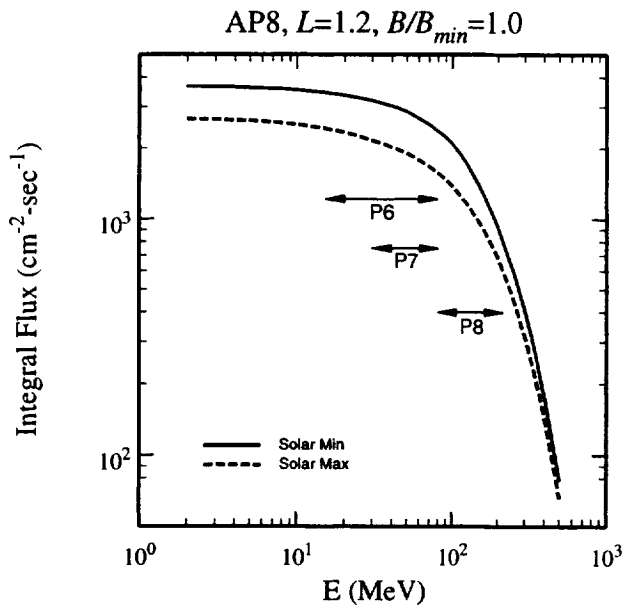


Figure 2-4. Proton energy spectra from AP8 MIN and MAX, showing the coverage of the MEPED omnidirectional detectors.

2.4 Instrument Analysis

We have performed an extensive analysis of the MEPED omnidirectional detectors in order to identify and quantify any instrumental effects which might affect the measured proton fluxes.

2.4.1 Detector Threshold and Particle Discrimination

As stated previously, the omni detectors consist of a silicon detector element beneath a hemispherical moderator dome. The dome absorbs protons and electrons below a given energy and lets higher-energy particles through to the detector element; thus, the dome determines the low-energy cutoff of the instrument. The particles

which strike the detector deposit a certain amount of energy in passing through or stopping within the detector. The instrument electronics use a simple threshold to determine whether or not to count an event. This thresholding can, in principle, determine the high-energy cutoff for the instrument and provide discrimination between protons and electrons.

Figure 2-5 shows the energy deposited in the silicon detector as a function of the free-space energy of a proton or an electron for all three channels. It can be seen that the low-energy cutoffs for protons occur at approximately 16, 36, and 80 MeV for the P6, P7, and P8 channels, respectively. For electrons the low-energy cutoffs are about 1, 4, and 22 MeV. Also shown in the figure is the 200 keV counting threshold. It can be seen that this threshold was not chosen very judiciously: it allows electrons to be detected, and it does not result in a high-energy cutoff for the protons. If the threshold had been set to 2 MeV, or conversely, if the detector thickness were reduced to 0.3 mm instead of 3 mm, the instrument would reject electrons, and the protons would have a high-energy cutoff of about 250 MeV, as the NOAA documentation states.

According to the AE8 electron model and the AP8 proton model, the P7 and P8 channels should not be affected by electron contamination, since electrons with energy greater than 4 MeV essentially do not exist in the inner zone. The situation is more complicated for the P6 channel, since AE8 predicts significant numbers of >1 MeV electrons; in some regions the electron flux can be more than ten times the proton flux. More recent data (Reference 12), however, show that AE8 significantly overpredicts the flux of high-energy electrons: at $L=1.4$, the CRRES data are more than a factor of ten lower than AE8. This reduced electron flux will permit the P6 channel to detect primarily protons. However, some contamination by electrons cannot be ruled out at

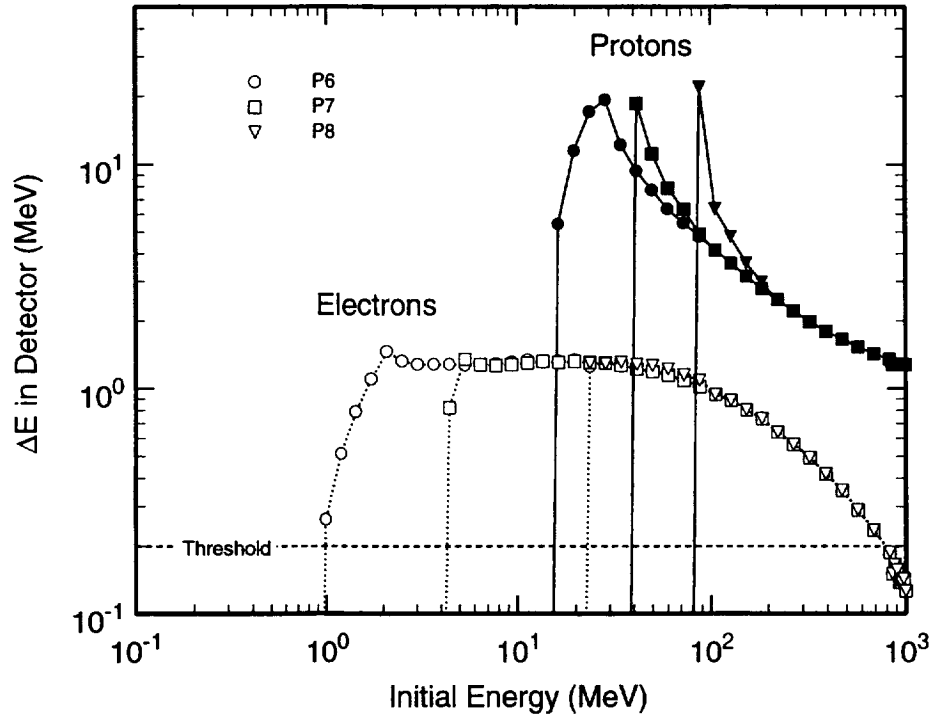


Figure 2-5. Plot of ΔE vs. E for the MEPED omnidirectional detectors.

this point. A better understanding of the inner-zone electron flux as a function of solar activity is required before correction factors for electron contamination can be estimated.

2.4.2 Secondary Production

We have performed a proton transport calculation using the BRYNTRN code (Reference 13) to determine the effect of secondary particles generated in the moderator dome. For a thickness of 10 g/cm^2 of tungsten, secondary protons are about two orders of magnitude less intense than the primary protons. Neutrons with energy greater than 2 MeV constitute about 5 percent of the total particle flux, but their interaction cross section is low, and we do not expect that they would contribute to the count rate.

Production and detection of Bremsstrahlung is a relatively inefficient process, with overall efficiencies on the order of 10^{-4} . Contamination of detectors by Bremsstrahlung is limited mainly to detectors with a small angular response. The MEPED omni detectors have a solid angle of nearly 2π , and thus the efficiency of Bremsstrahlung detection is many orders of magnitude less than the direct detection of protons.

2.4.3 Energy Cutoffs

Uncertainties in the actual values of the upper and lower energy cutoffs for each channel will lead to uncertainties in the measured flux. If the energy range of particles actually detected is

larger than the advertised energy range, the measured flux will be too large. We have determined the minimum energy for protons penetrating the shields for the three channels and used these as the low-energy cutoff energy; our values agree with the advertised values. These values pertain to a point at the exact center of a perfect hemispherical shell. In reality, the detector has a finite size, and the shell is not a perfect hemisphere; these geometric considerations will lead to some uncertainty in the actual cutoff energies. This uncertainty will have a minimal effect on the accuracy of the instruments, because the proton spectrum near 80 MeV and below is very flat (see Figure 2-3), and thus the count rate is relatively insensitive to the cutoff energy. Reducing the P8 lower cutoff to 50 MeV, for example, would change the calibration by only about 25 percent. The P6 and P7 channels are even less sensitive to this error source.

The largest uncertainty arises from particles entering the detector from the spacecraft side (*i.e.*, the nadir direction). The detectors are shielded from behind by the spacecraft mass as well as some additional Mallory shielding. During the detector design process, it was assumed that this shielding amounted to about 12 g/cm², which is reflected in the selection of 11.5 g/cm² for the P8 moderator. The idea was to make the P8 channel as close to a truly omnidirectional detector as possible for >80 MeV protons

We have assumed that the back-side shielding approximates a hemispherical shell of 11.5 g/cm², and thus that the P8 detector approximates a true omnidirectional detector. If the effective shielding were actually 6 g/cm², the back side shielding would stop protons with energies less than about 55 MeV, and the actual flux would be about 9% higher than for a true omnidirectional detector. If the effective shielding from behind were actually 24 g/cm², it would stop protons with energies less than about 120 MeV, and the actual flux would be about 14% less than for a true omnidirectional detector.

2.4.4 Geometric Factor

In the following discussion of detector efficiency we focus on the effect of the non-isotropic flux distribution on the overall efficiency of the detector. We are able to calculate the geometric efficiency for both an isotropic flux (this calculation agrees with the published value of 0.215 for the omnidirectional flux) and for the actual flux distribution present in the radiation belt. The maximum error introduced by using an efficiency based on an isotropic distribution is less than 20 percent. The resultant directional efficiency is primarily a function of the angle between the detector and the magnetic field. The efficiency is very insensitive to the assumed shape of the pitch angle distribution.

Isotropic Flux

Let f be the directional flux in units of particles/cm²-sec-sr, and let F be the omnidirectional flux in units of particles/cm²-sec. If f is independent of the polar angle \angle and azimuthal angle θ (*i.e.*, the flux is isotropic), we can write:

$$F = \int_0^{2\pi} \int_0^\pi f \sin \varphi d\varphi d\theta = 4\pi f$$

Assuming a detector efficiency of 1.0, for a spherical detector of cross sectional area A , the count rate C is given by

$$C = \int_0^{2\pi} \int_0^\pi fA \sin \varphi d\varphi d\theta = 4\pi Af$$

Thus

$$F = \frac{C}{A}$$

For a flat circular detector of cross sectional area A , the count rate is given by

$$C = \int_0^{2\pi} \int_0^\pi fA \cos \varphi \sin \varphi d\varphi d\theta = 2\pi Af$$

Thus

$$F = 2 \frac{C}{A}$$

Pitch Angle Dependent Flux

Let us assume we have a pitch angle dependent flux that has the form

$$f(\alpha) = f_0 g(\alpha)$$

where $g(\alpha)$ is a function which varies between 0 and 1 and gives the relative intensity of the flux as a function of look angle with respect to the magnetic field. The total flux F is then given by

$$F = \int_0^{2\pi} \int_0^\pi f_0 g(\alpha) \sin \varphi d\varphi d\theta = bf_0$$

where

$$b = \int_0^{2\pi} \int_0^\pi g(\alpha) \sin \varphi d\varphi d\theta$$

Thus

$$f_0 = \frac{F}{b}$$

So for a flat circular detector of area A , the count rate C measured by the detector is given by

$$\begin{aligned} C &= \int_0^{2\pi} \int_0^{\pi} f_0 g(\alpha) A \cos \varphi \sin \varphi d\varphi d\theta \\ &= \frac{F}{b} A \int_0^{2\pi} \int_0^{\pi} g(\alpha) \cos \varphi \sin \varphi d\varphi d\theta \end{aligned}$$

Thus,

$$F = \left(\frac{b}{d} \right) \frac{C}{A}$$

where

$$d = \int_0^{2\pi} \int_0^{\pi} g(\alpha) \cos \varphi \sin \varphi d\varphi d\theta$$

The constant b/d is only slightly sensitive to the exact shape of the pitch angle distribution and is somewhat sensitive to the direction of the magnetic line of force relative to the detector surface. The NOAA detectors always face the zenith and thus the plane of the detector is parallel to the surface of the Earth. Therefore, near the equator, at $B/B_{\min}=1.0$, the magnetic field vector lies in the plane of the detector. At $B/B_{\min}=2.0$, the magnetic dip angle is much greater, and the magnetic field vector makes an angle of about 40 degrees to the plane of the detector. We developed a simple FORTRAN computer code that used a DATA statement to enter a pitch angle function, $g(\alpha)$, for both $B/B_{\min}=1.0$ and $B/B_{\min}=2.0$. The pitch angle distribution at $B/B_{\min}=2.0$ is much narrower. The computer code was then used to calculate the double integrals for b and d .

When the magnetic field is in the plane of the detector, the constant $b/d=1.62$ when we used a pitch angle distribution with a 65 degree loss cone, and changes to 1.59 for an 80 degree loss cone. It is very insensitive to the shape of the pitch angle distribution. When the magnetic field makes a 40 degree angle with the surface of the detector, the constant $b/d=2.05$ and is similarly insensitive to the shape of the pitch angle distribution. Thus the geometry factor of the detector changes by approximately 20% over the region for which we have data. The detector is slightly more efficient in counting protons near the magnetic equator, since fewer protons make an oblique angle with the detector.

2.4.5 Detector Efficiency

Electron detectors can have efficiencies less than unity because of backscattering. Proton detectors, however, do not suffer from this problem. If a proton has sufficient energy to enter a detector element and loses sufficient energy to be counted, its probability of detection is essentially unity. Except for dead-time corrections, no significant detector efficiency losses need be included for proton detectors.

2.4.6 Data Quantization

Because the count rates are packed before the data are telemetered to Earth, there is some inherent granularity in the unpacked data. For count rates greater than 32 counts per accumulation interval, the counts are quantized, with the width of each bin approximately 4% of the average value for the bin. There is therefore an inherent uncertainty of about 4% in the data, but no overall bias is introduced.

2.4.7 Summary of Instrument Analysis

Table 4 summarizes the various sources of errors discussed above.

2.5 Data Archive

SEM data are received in near real-time by the Space Environment Services Center (SESC) of the Space Environment Laboratory in Boulder, Colorado. The raw data are processed and re-formatted every ten days. The data are used operationally by SESC, and are archived every month in binary format on 3480 magnetic tape cartridges. The archive processing calculates certain values (e.g., ephemeris and magnetic field), reformats the raw telemetry data, and packs all information into 8-second logical records. The data are available on tape or CD-ROM from

Table 4. Summary of error sources for the MEPED instrument. Note: an error estimate of +10% indicates that the measurement overestimates the true flux by 10%.

Effect	Estimated Error (%)	Comments
Electron Contamination	?	Essentially zero for P7 & P8; unknown for P6
Secondary Production	0	
Energy Cutoff	±10	
Geometry Factor	+20	Error highest at largest B/B_{\min} , generally less than +20%
Detector Efficiency	±10	Essentially unity
Quantization	±4	

the National Geophysical Data Center (NGDC). Each data file contains from 8 to 11 days of data and is approximately 30 megabytes long. Reference 10 contains a detailed description of the archive format; we give a much abbreviated description here.

Each 8-second logical record contains 332 bytes. A logical record contains the following information:

- Orbital information (time, latitude, longitude, magnetic coordinates, etc.).
- Total energy flux values from the TED instrument.
- Spacecraft housekeeping information (instrument temperatures, etc.).
- Instrument status and calibration flags (indicating whether an instrument is on or off or undergoing in-flight calibration).
- MEPED data.
- HEPAD data (for TIROS-N, NOAA-6, and NOAA-7).
- TED data.

The three instruments are actually sampled every two seconds, so each 8-second logical record contains data for four 2-second sampling intervals.

3. DATA PROCESSING

The data archive files contain approximately 500,000 individual raw, packed data records. In order to analyze and model the data it is necessary to extract the raw data to a uniform grid in B/B_{\min} , L , and time (or solar flux). It is also necessary to identify and compensate for any artifacts in the data due to the characteristics of the instruments or data processing. This section discusses our data processing techniques.

3.1 *Generation of Corrected Data Files*

In order to simplify the data processing procedure, we first developed a computer program called NOAACOR.EXE which performs the following functions:

1. read a logical record from the archive file
2. sum the data from each 2-second sampling interval to obtain 8-second data (MEPED instrument only)
3. compute spacecraft position and magnetic field parameters
4. write a re-formatted binary record to a new “corrected” data file

The following sections discuss each of these steps in some detail, since this pre-processing is critical to understanding the data.

3.1.1 Read Logical Record

Each logical record is read into a C structure; the data are unpacked into physical units and count rates (contained in another C structure) using the *decode()* function supplied by NGDC.

3.1.2 Data Summing

For the MEPED instrument, each 8-second logical record contains data for four 2-second accumulation intervals for each of the 19 proton and electron channels. (The 0° and 90° ion channels are read out every 16 seconds.) The counts for each channel are packed and stored as one-byte integers. In order to get better counting statistics and to reduce the size of the data files, we sum the counts for the four accumulation intervals to obtain 8-second time resolution. In order to do this, we unpack the counts for each channel and accumulation interval, sum them, and re-pack the summed counts.

This summing process also allows us to perform some error detection and correction. For each channel, we have a four-element vector containing the counts from each 2-second accumulation interval. We first compare the largest and smallest elements; if the ratio between them is less than a test value, all four elements are assumed to be good, and the sum is returned. If the ratio is

larger than the test value, we test to see if one of the elements is different from the other three. First, the largest element is rejected and the range of the other three elements is tested. Then the smallest element is rejected and again the range of the other three is tested. If either of these secondary tests meets the criteria, the “bad” element is rejected and the function returns a value of 4/3 times the sum of the remaining three elements (*i.e.*, we assume the “bad” point would have had a value equal to the average of the other three). If the secondary tests do not meet the criteria (*i.e.*, there were more than two “bad” values), the entire 8-second interval is assumed to be bad and is flagged. These tests are performed for all 19 proton and electron channels.

3.1.3 Compute New Position and Magnetic Field Parameters

This step is the most crucial of the pre-processing procedure. The archive files contain the spacecraft latitude, longitude, vector magnetic field, and magnetic L value. The magnetic field and L , however, are determined by a simple table lookup (Reference 11) based on an assumed spacecraft altitude of 870 km. Early in our analysis procedure, we extracted data directly from the archive files and plotted the omnidirectional count rate as a function of magnetic field strength for a given L -value; typical results are shown in Figure 3-1. There is a great deal of scatter in the data, and the measurements from the two spacecraft do not agree.

Eventually, it was determined that the problem was caused by the procedure used to determine the magnetic coordinates. Given the large gradients in the trapped particle flux in the region of interest, the magnetic coordinates on the archive files were not accurate enough for our purpose. We therefore re-computed the B , L coordinates. First, we re-computed the spacecraft position (in order to determine the actual altitude) using the SGP4 ephemeris model (Reference 14) and spacecraft orbital elements which are archived on the Internet. The latitude and longitude calculated using SGP4 usually matched those on the archive tapes to within about 0.01 degrees. However, re-calculating the ephemeris allowed us to determine the spacecraft altitude, which made the subsequent B , L calculations more accurate.

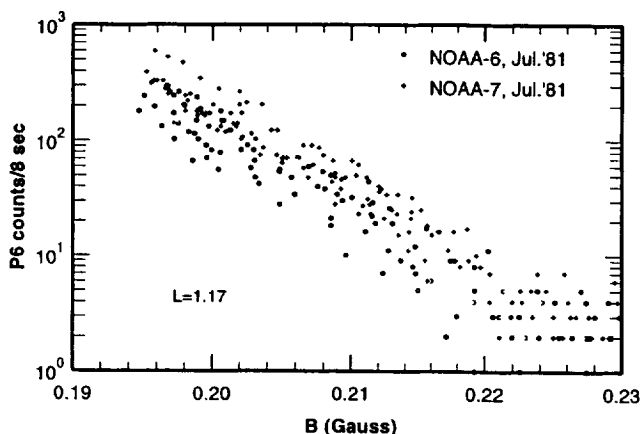


Figure 3-1. Example of data using B , L coordinates from NOAA archive file.

The B - L calculation procedure was developed by Pfitzer (Reference 15) for the CRRES data analysis. It uses a fourth order Runge-Kutta integration technique with variable step size and selectable error control. The program is designed to work with the IGRF internal field model (Reference 16); an option allows it to include the external field and determine the L value for particles of different pitch angles (this option was not used for this analysis). The IGRF code has been modified to drop the higher order terms as a function of altitude; the coefficients are

updated to the ephemeris month. Accuracy in the field expansion with term dropping is maintained to better than one nanotesla. The integration routine determines the actual minimum value of the magnetic field along the integration path when determining the second invariant. The value of L is calculated using the expansion of Hilton (Reference 17) and uses the dipole moment as determined from the IGRF model used in the invariant calculation. The code has been extensively tested against the original code written by McIlwain (Reference 18)

and has been used extensively in the analysis of the CRRES data. Figure 3-2 shows the same data as Figure 3-1, but after the data processing; the quality of the data has clearly improved.

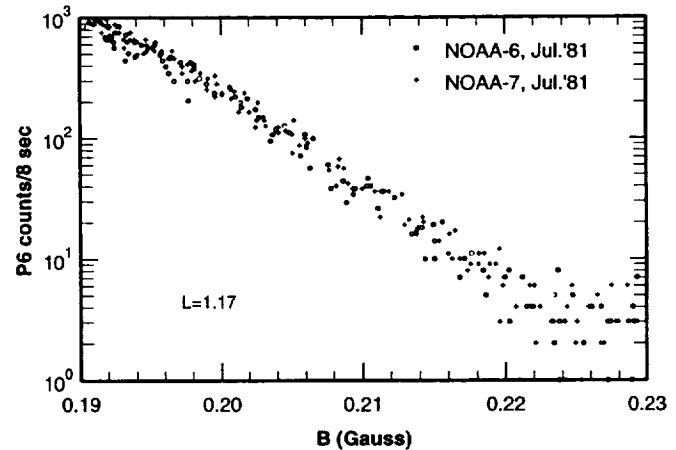


Figure 3-2. Same data as Figure 3-1, but organized using new B, L procedure.

In addition to the steps listed above, we also compute the pitch angles of the particle telescopes based on the IGRF magnetic field.

3.1.4 Create New Archive File

Once all this pre-processing is finished, a new packed binary file containing the corrected magnetic coordinates and 8-second count rates is created. These files are typically about 5 megabytes in size. We also developed a program called RDCOR.EXE which reads these files and extracts data within a range of criteria specified by the user. Appendix C describes this program and the format of the corrected data files.

3.2 Time Shift

Even once the corrected B, L coordinates were calculated, we found a residual source of scatter in some of the data files. Figure 3-3a shows an example; there is a clear bifurcation in the data. Upon further analysis, we determined that one leg of the curve resulted from northbound passes of the satellite, and the other leg resulted when the spacecraft was southbound. The simplest explanation for this type of behavior is an ephemeris timing error. For example, the spacecraft clock controlling the data timing is not synchronized with the clock with which the spacecraft ephemeris is generated. This behavior is surprising since the positions we calculated were so close to those on the archive files. Actually, a small time shift is to be expected, since the center of the 8-second data accumulation interval occurs two seconds after the ephemeris time. In order to obtain the best data quality, we scanned each corrected data file and determined a time shift which resulted in the minimum scatter. Figure 3-3b shows the same data as Figure 3-3a, with a time shift of -16 seconds.

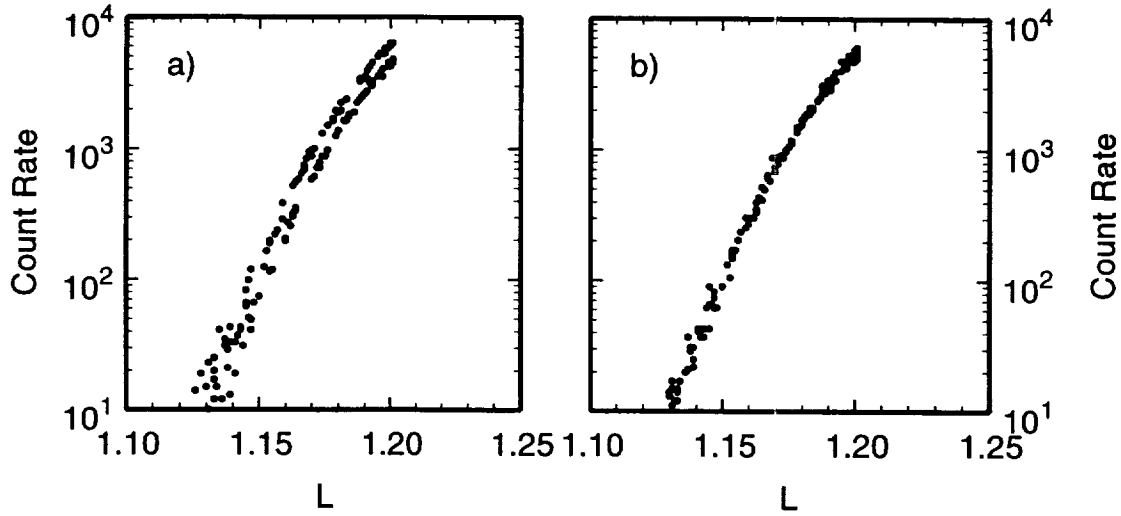


Figure 3-3. (a) Count rate as a function of L for $B/B_{\min}=1.0$, with no time shift introduced. Note the bifurcation in the data. (b) Same data with a time shift of -16 seconds applied.

3.3 Detector Backgrounds

Detector backgrounds were estimated by extracting data from the region labeled “counts below background” in Figure 2-3 and averaging them. The results are shown in Figure 3-4. The background count rate is quite consistent over the data period and among spacecraft. Some modulation of the count rate is seen, out of phase with the solar $F_{10.7}$ flux, indicating that the background counts may be due to galactic cosmic rays. We have assumed a constant background count rate of 3 counts per 8-second interval, and have subtracted this value from the count rates in subsequent analyses.

3.4 Data Grid

In order to facilitate the development and implementation of the model, we used a data grid which is a re-mapping of the traditional B/B_{\min} , L space. In place of B/B_{\min} , we used the parameter ζ , defined as

$$\zeta = \sin^{-1} \left[\left(B / B_{\min} \right)^{-1/2} \right].$$

Physically, ζ is the equatorial pitch angle of a particle mirroring at a given value of B/B_{\min} ; we adopted this parameter because it stretches out the grid as B/B_{\min} increases. At the geomagnetic equator ($B/B_{\min}=0$), $\zeta=90^\circ$.

In place of L , we use a parameter $L'=L-S$, where S is the value of L at the Earth's surface for a given value of ζ (or B/B_{\min}). We have approximated S using the equation

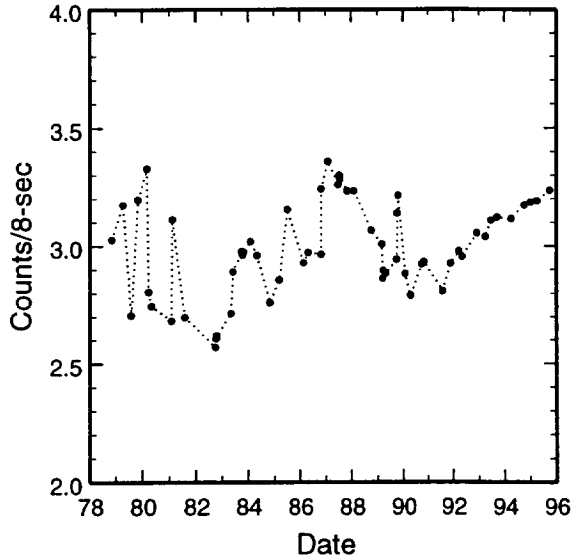


Figure 3-4. Average background count rate in counts per 8 second interval for the period 1978 – 1995.

binning and averaging technique for several reasons. The data points are distributed non-uniformly in ζ - L' space, so that in order to obtain a statistically meaningful number of points at larger values of ζ , larger bins must be used. The smoothing procedure effectively fits a surface to a fraction of the total data set (in this case approximately 10%) closest to the point in question, and thus in effect automatically increases the size of the “bin” while also accounting for the trend of the data within the “bin”. The procedure can output smoothed values for both the input data points and an arbitrary grid. Smoothing was performed on the natural logarithm of the count rate for each of the three channels, with the background counts subtracted.

$$S = 1.1(B/B_{\min})^{0.3048}.$$

The data grid selected is uniform in both ζ and L' , with ζ ranging from 20 to 90 degrees in steps of 2 degrees. L' ranges from 0.02 to 0.20 Earth radii in steps of 0.01 R_E . Figures 3-5 and 3-6 show the model grid in ζ - L' space and in B/B_{\min} , L space.

3.5 Data Smoothing

Using the corrected data, we next applied a two-dimensional local regression (lowess) smoothing procedure (Reference 19) to smooth the data in ζ - L' space and output the results on a uniform grid. We use this procedure rather than the more traditional

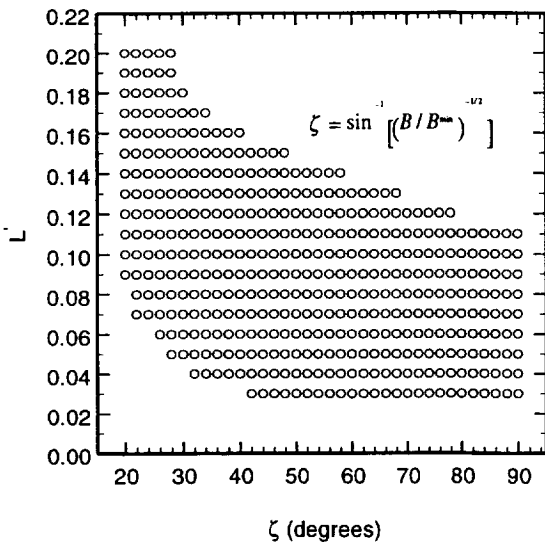


Figure 3-5. Model grid in ζ - L' space. The points indicate where MEPED data are available.

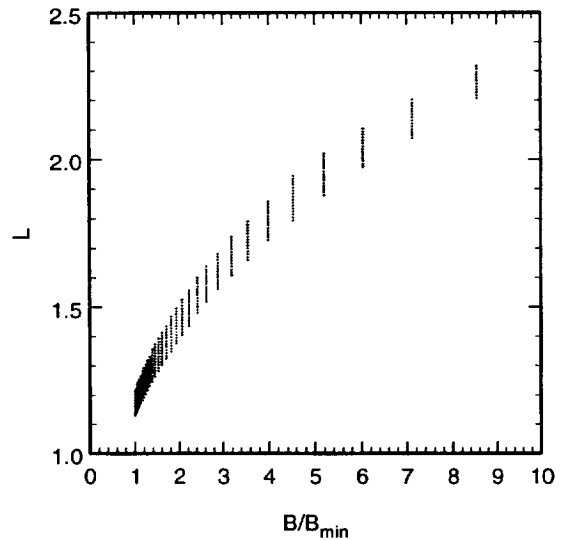


Figure 3-6. Model grid in B/B_{\min} - L space.

The smoothing procedure provides an estimate of the standard error of the residuals, which gives an idea of the scatter in the data and the quality of the smoothing. The standard error estimate typically ranged from 0.1 to 0.2, meaning that the smoothed points were typically within 10–20% of the actual value. Overall, about 80% of the smoothed values were within 35% of the actual values.

4. DATA ANALYSIS

We have performed a detailed analysis of the entire data set to determine the solar cycle variations of the 80–215 MeV trapped proton flux. The data presented in this section use the smoothed ten-day averages discussed in the previous section. This analysis has been submitted for publication (Reference 4).

4.1 Temporal Variations

Figure 4-1 shows the measured proton flux for various values of L at the geomagnetic equator as a function of time from 1978 through 1995. Each data point represents a 10-day average, with lowess smoothing using the procedure discussed above. Also shown for reference is the solar $F_{10.7}$ flux. The data cover two solar maxima and one solar minimum (and approaching a second minimum), with two periods of recovery of the proton flux. Several points are noted:

1. The proton flux shows a clear variation over the solar cycle, as expected. The difference between minimum and maximum varies from a factor of 5 at $L = 1.14$ to about 50% at $L = 1.20$.
2. The peak proton flux follows solar minimum by about a year at low L to two years at higher L .
3. The proton flux exhibits a rather broad minimum, and also seems to lag the maximum in $F_{10.7}$.
4. The flux decreases more rapidly approaching solar maximum than it increases approaching solar minimum.
5. The flux maximum which occurred prior to 1978 may have been somewhat higher than that measured in 1987. The flux minimum measured in 1990–1992 was lower than the one measured in 1980–1983.
6. The variation is quite smooth over time, but sharp transient peaks are observed, particularly in March and April 1991, corresponding to solar particle events (SPEs). These peaks are apparent even at very low L values.

The first four observations are consistent with models of the proton flux variation (*e.g.*, Reference 20).

Figure 4-2 shows a similar plot, but for $B/B_{\min} = 2.0$, and at higher L values. The solar cycle variation is again evident, but is somewhat more variable on smaller time scales. In particular, the effects of SPEs in March and October 1989 and other times are quite apparent. (Although the figure shows a long increase between the March and October 1989 events, the effect of these events may be relatively brief. We have not analyzed any data in the period between these events, so we can not yet make any comment on the decay time.)

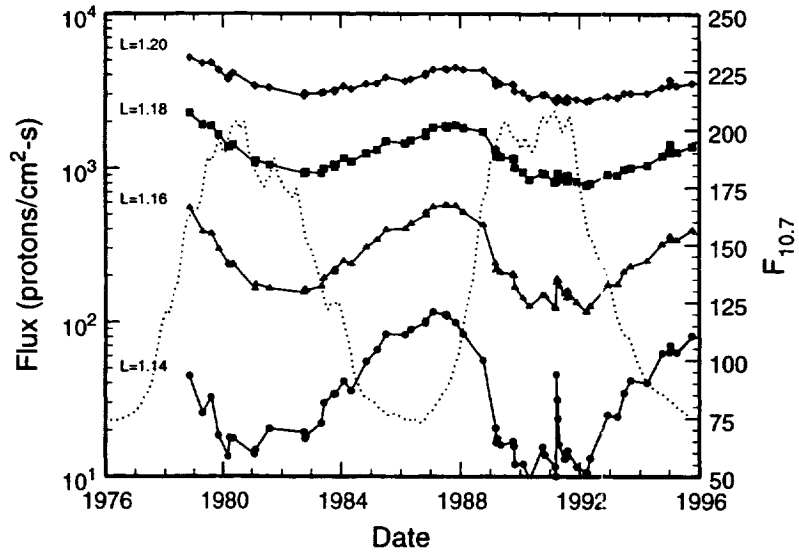


Figure 4-1. Temporal variation of the >80 MeV proton flux for several values of L at the geomagnetic equator ($B/B_{min}=1.0$). The dashed curve shows the solar $F_{10.7}$ flux for the same period.

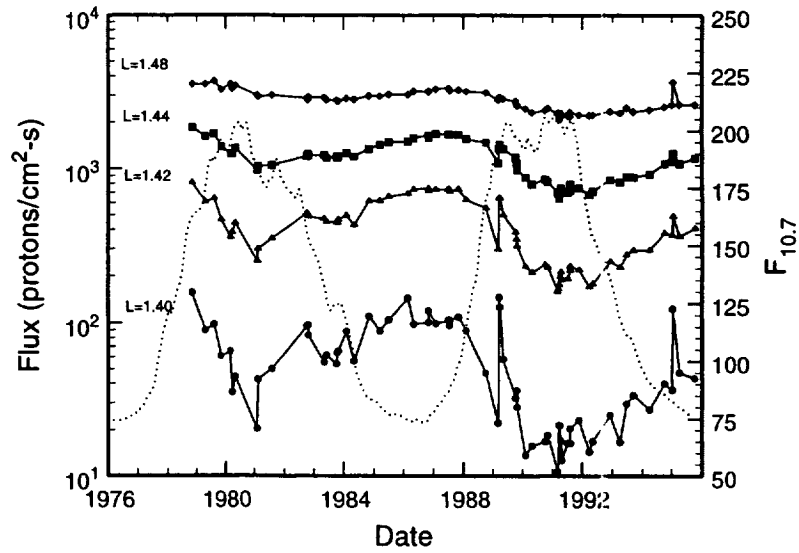


Figure 4-2. Temporal variation of the >80 MeV proton flux for several values of L at $B/B_{min}=2.0$.

4.2 Variations with Solar Activity

Figures 4-3 and 4-4 show the same data, plotted as a function of $F_{10.7}$. These figures show a clear hysteresis between the rising and falling portions of the cycle. At low L , the two recovery periods are quite similar; the flux remains approximately constant after solar maximum until $F_{10.7}$ falls below about 160. At higher L , particularly for the curves shown in Figure 4-4, the two recovery periods are quite different. Proton fluxes for the 1982–1986 recovery period are as

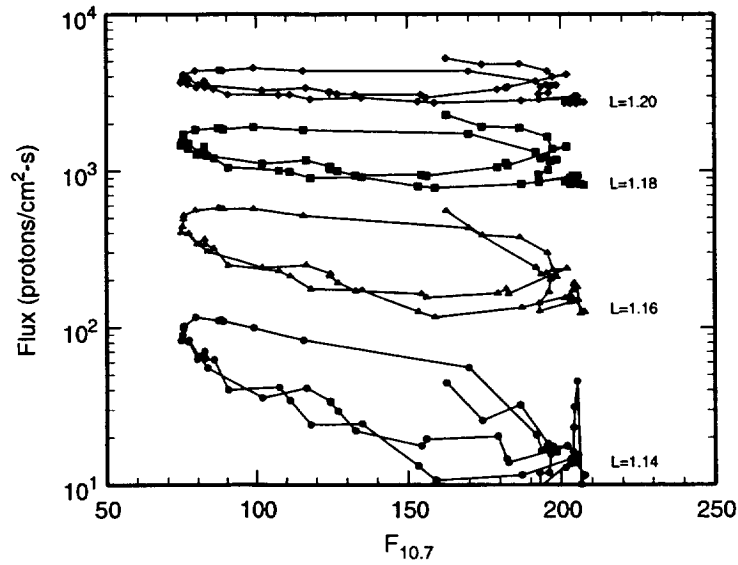


Figure 4-4. Variation of the >80 MeV proton flux with solar activity for several values of L at the geomagnetic equator ($B/B_{min}=1.0$).

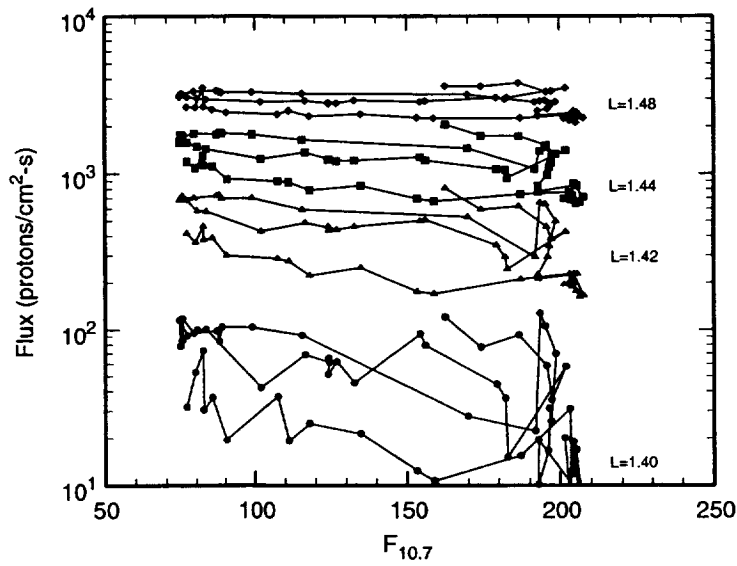


Figure 4-3. Variation of the >80 MeV proton flux with solar activity for several values of L at $B/B_{min}=2.0$

much as a factor of 2 higher than fluxes in the 1992–1995 recovery period.

The difference between the recovery periods may be explained by the fact that the maximum of solar cycle 20 (around 1970) was rather small, with a maximum $F_{10.7}$ of about 150. With low solar activity, the inner zone proton flux would not have been depleted as much as in cycles 21 and 22. Thus, during the recovery period between 1970 and 1978, the proton flux may have risen to levels considerably higher than those seen in 1987 and 1995. Changes in the position of the B , L coordinate system relative to the surface of the Earth, due to secular changes in the Earth's

magnetic field, may also account for some of the observed differences. Much additional work is required in order to understand this trend in the data.

4.3 Solar Particle Events

Sharp enhancements in the proton flux are seen in 1989 (twice) and 1991, corresponding to SPEs in March and October 1989 and March 1991. Other possible enhancements are noted in 1982, 1983, and 1995, although these have not yet been identified with specific SPEs. The 1991 enhancement is discernible at all values of L , particularly at low L (Figure 4-1), while the 1989 enhancements are most obvious at larger values of L (Figure 4-2).

Our data set currently does not have sufficient time resolution to discuss these enhancements in detail. For example, we have not analyzed any data between March and October 1989, so it is not possible to state at this point whether the flux decreases or remains elevated between these events. The 1991 enhancement appears to decay quite rapidly (approximately 30 days), followed by a more gradual decay (perhaps a year). Further study is required in order to determine the mechanism for these increases. Electron contamination is unlikely, for the reasons noted in Section 2.

4.4 Pitch Angle Distributions

The atmospheric density encountered by individual particles is a function not only of the L shell on which a particle resides but also of the particle's mirror point, *i.e.*, the pitch angle distribution. For those L shells for which we have a complete omnidirectional directional flux profile along the entire field line, it is possible to invert the data and produce plots of flux versus equatorial pitch angle. Figure 4-5 shows the omnidirectional flux at $L = 1.2$ as a function of B/B_{\min} . Figure 4-6 shows the equatorial pitch angle distribution for $L = 1.2$ for solar minimum and solar maximum derived from the omnidirectional curves in Figure 4-5. The omnidirectional curves show a 75% increase in the $B/B_{\min} = 1.0$ flux at solar minimum with respect to solar maximum. The directional data show that the particles that mirror at the equator (equatorial pitch angle = 90°) increase by less than 25%. The difference between solar maximum and solar minimum is a strong function of the particle's pitch angle. Thus in order to develop a useful engineering model, it may be necessary to model the changes in directional flux as a function of L and atmospheric density and then convert to omnidirectional flux. Note that, for this data set, pitch angles can be determined only for $L < 1.22$, the maximum value for which the spacecraft reaches the geomagnetic equator.

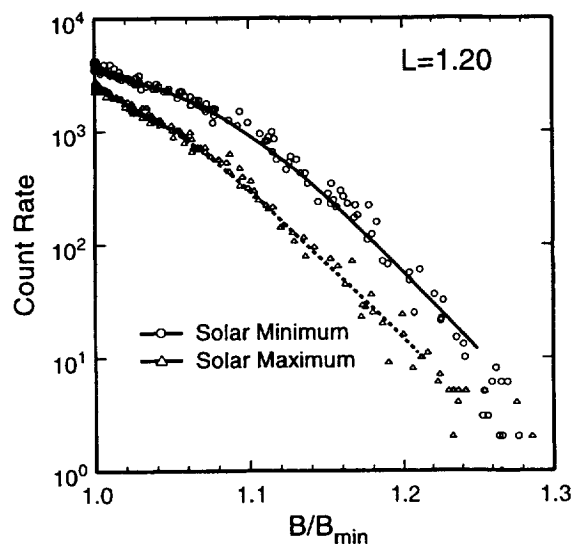


Figure 4-5. Omnidirectional count rate as a function of B/B_{\min} at $L=1.2$ for solar minimum and solar maximum conditions.

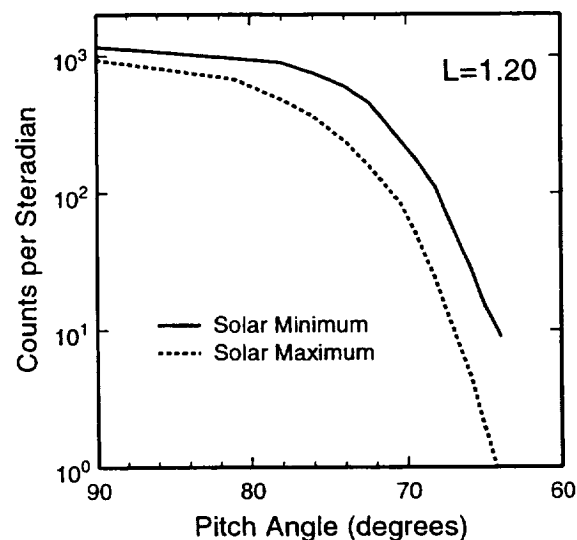


Figure 4-6. Pitch angle distributions for $L=1.2$ at solar minimum and solar maximum determined using the omnidirectional flux distributions shown in the previous figure.

4.5 Intercomparison of Spacecraft

In selecting the data for analysis, we selected several intervals in which two spacecraft were taking data simultaneously, in order to ensure that data from different spacecraft were comparable. Figures 4-7 through 4-10 compare the P8 channel count rate as a function of L at the geomagnetic equator for four periods in which there was data overlap. It can be seen that the count rates compare quite well, within the data scatter from an individual instrument. The data used for comparing NOAA-14 with NOAA-12 were from the first month of operation of NOAA-14, and the early data show a constant count rate of 4216 counts per 8-seconds. Data from 11 January through 18 January 1995 are excluded from Figure 4-10. Although Figure 4-10 shows only 2 days of data for NOAA-14, these data also compare well with the NOAA-12 data.

We therefore conclude that the calibration factors for the instruments are quite consistent from spacecraft to spacecraft. The calibration factors do not appear to change with time (*e.g.*, NOAA-6 had been in space for over six years during the interval where the data are compared with NOAA-10).

4.6 Comparison with AP8

Figure 4-11 compares the fluxes obtained from the MEPED P8 channel with the >80 MeV integral flux predictions from AP8 at several values of B/B_{\min} . The NOAA data are consistently and significantly higher than the AP8 model. Ironically, AP8 agrees with the data best at low

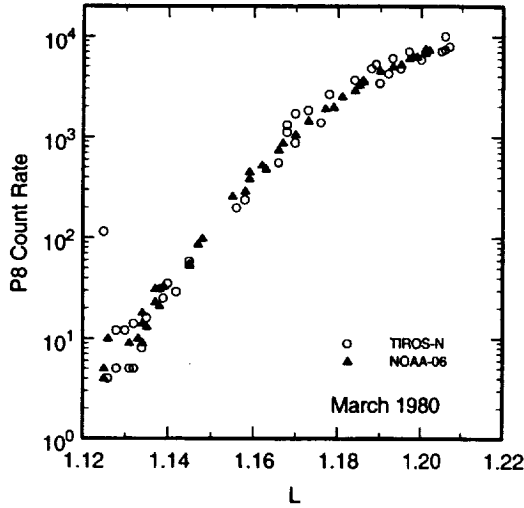


Figure 4-7. Comparison of P8 count rates measured by TIROS-N and NOAA-6 at the geomagnetic equator in March 1980.

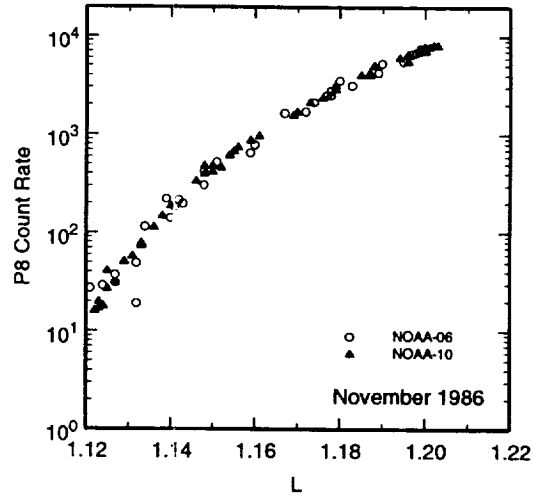


Figure 4-8. Comparison of P8 count rates measured by NOAA-6 and NOAA-10 at the geomagnetic equator in March 1980.

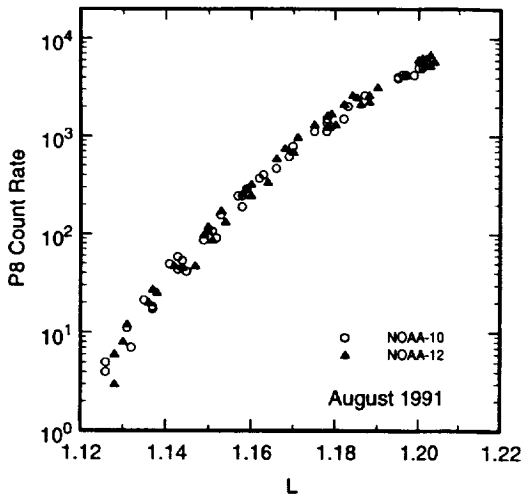


Figure 4-9. Comparison of P8 count rates measured by NOAA-10 and NOAA-12 at the geomagnetic equator in March 1980.

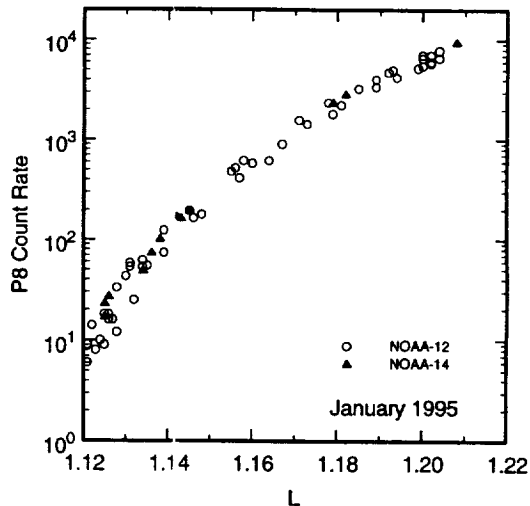


Figure 4-10. Comparison of P8 count rates measured by NOAA-12 and NOAA-14 at the geomagnetic equator in March 1980.

values of L , near the atmospheric cutoff. Section 4 contains further comparisons between AP8 and the NOAAPRO model.

4.7 NOAA-10 Data Anomaly

Figure 4-12 shows the count rate as a function of time for the P5, P7, and P8 channels at $\zeta=80^\circ$, $L'=0.10$. The P7 count rate is seen to lie in between P6 and P8 (as expected) until late in 1986. It then drops sharply and, except for a few points, tracks the P8 count rate almost exactly. Then late in 1991, the P7 count rate increases sharply and once again lies in between P6 and P8. Similar behavior is seen at other values of ζ and L' . Upon further investigation, we determined

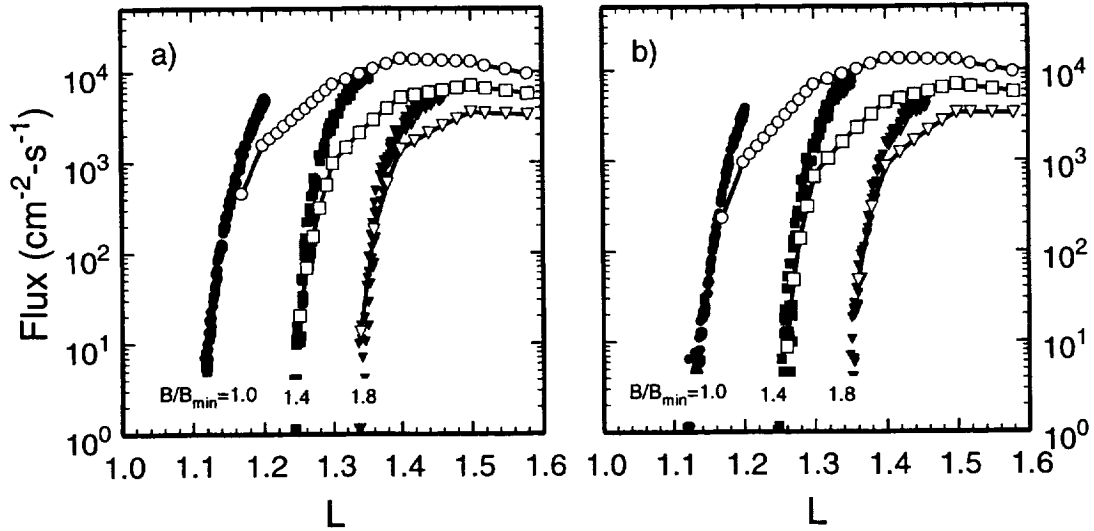


Figure 4-11. Comparison of measured >80 MeV proton fluxes with AP8 predictions. a) Solar minimum. b) Solar maximum. Solid symbols show NOAA data; open symbols/lines show AP8 predictions.

that all the anomalous points came from the NOAA-10 spacecraft. We also determined that the smoothed P7 count rates were similar to, but not identical to, the smoothed P8 count rates.

After extensive discussions with Dr. David Evans at the NOAA Space Environment Center about this issue, the reason for the anomalous behavior remains unclear. If the P7 and P8 count rates were identical, we could say that the telemetry was somehow transmitting the P8 counts twice. Since the two count rates are slightly different, there are two distinct data streams being transmitted. One possible explanation for the behavior is that the P7 and P8 detectors both have identical moderator domes (11.5 g/cm^2 Mallory).

Because of the anomalous behavior, we have excluded NOAA-10 P7 data from our model. The data from the P6 and P8 channels on NOAA-10 appear good and compare well with data from NOAA-6 and NOAA-12. These data are included in the model.

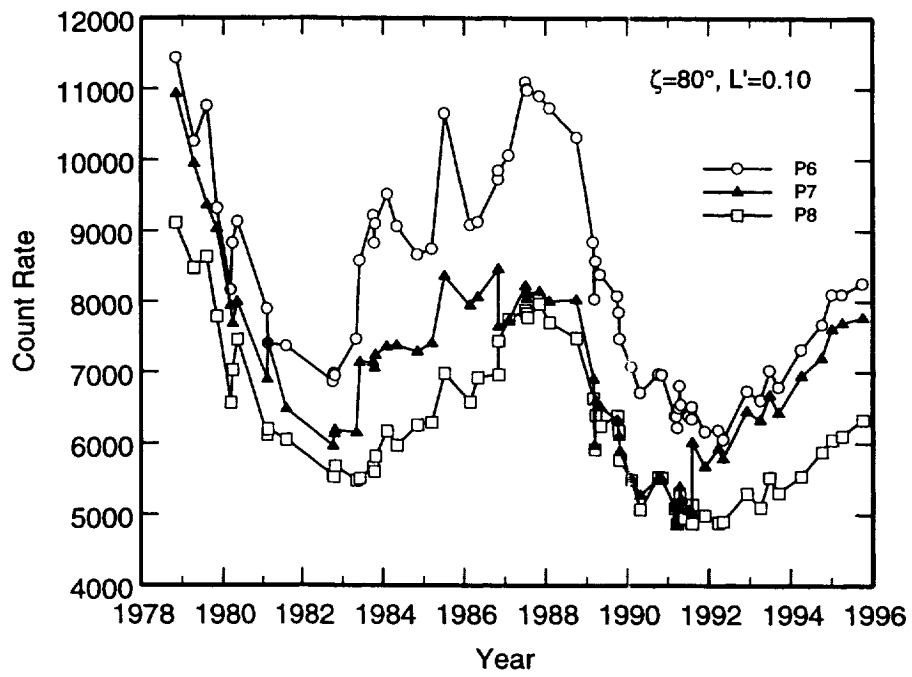


Figure 4-12. Count rates in the P6, P7, and P8 channels as a function of time. Note the sharp drop in the P7 count rate in 1986 and the sharp increase in 1991.

5. MODEL DEVELOPMENT

Our original plan for this study was to develop a new coordinate system based on atmospheric density, along the lines of those presented in References 21 and 22. Based on the analysis of the previous section, this approach does not appear to be feasible at this time.

The large hysteresis in the flux (*e.g.*, Figures 4-4 and 4-5) shows that the flux is not a single-valued function of $F_{10.7}$, the atmospheric density, or any other simple function of the current value of these parameters. Instead, the flux depends on the past history of the particle source and loss mechanisms. In addition, there is a possible secular decrease in the flux which may be due to the secular changes in the Earth's internal magnetic field.

Therefore, we have adopted a somewhat simplified approach in which we determine the phase lag between the count rate in each of the three channels and $F_{10.7}$ and use a simple exponential curve fit to describe the relation between the proton flux and the phase-shifted $F_{10.7}$. This approach has the advantage of reproducing approximately the phase lag and is quite efficient in terms of computational and data storage requirements. It also results in a set of model parameters which give some insight into the physical processes controlling the proton flux.

5.1 Determination of Model Parameters

To develop the model, we first combined the smoothed, gridded flux data for all 67 data files into one large file. For each point in ζ - L' space, we then extracted all the data points to obtain the proton flux as a function of time. We then determined a phase lag τ which minimized the residuals from a curve fit of the form

$$\ln(C) = a_0 + a_1 F'_{10.7}$$

where C is the count rate and $F'_{10.7}$ is the value of $F_{10.7}$ which existed at time $(t-\tau)$, where t is the date at which the measurement was taken. The parameters τ , a_0 , and a_1 were determined by first assuming a phase lag τ . The linear curve fit was then performed and the parameter χ^2 , which is related to the variance of the residuals (see Reference 23) was determined. The process was then repeated for different values of τ , and the values of τ , a_0 , and a_1 which minimized χ^2 were selected. Figure 5-1 shows the variation of χ^2 , a_0 , and a_1 with the assumed phase lag τ for one value of ζ and L' . The procedure is repeated for all three energy channels.

Figures 5-2 through 5-4 show contours of τ , a_0 , and a_1 in ζ - L' space for the P8 (>80 MeV) channel. As expected, the phase lag increases with increasing L' near the equator ($\zeta > 50^\circ$). Near the upper limit of L' , the computed phase lag starts to decrease. This effect is an artifact due to the decreasing dependence on $F_{10.7}$ at high L' . As seen in Figure 5-4, the parameter a_1 , which represents the dependence on $F_{10.7}$, approaches zero at high L' , as expected. Thus the

phase lag starts to have no significance – if the flux is not a function of $F_{10.7}$, one phase lag is as good as another. We see two competing effects: as the phase lag increases, the solar cycle effect decreases.

The parameters τ , a_0 , and a_1 show similar variations for the P6 and P7 channels. Note, however, that the count rates for these channels include the P8 response. Remember also that these are integral channels and thus contain a wide range of proton energies. From this data set, it is difficult to draw any definitive conclusions about, for example, the phase lag for 16 MeV protons vs. that for 80 MeV protons.

Note that the largest values (numerically) of a_1 found for the P8 channel are about 0.015. For a solar cycle where $F_{10.7}$ varies between 70 and 200, this value of a_1 corresponds to a factor of 7 difference between the proton fluxes at solar minimum and solar maximum. The largest phase lags found for the P8 channel were about 24 months.

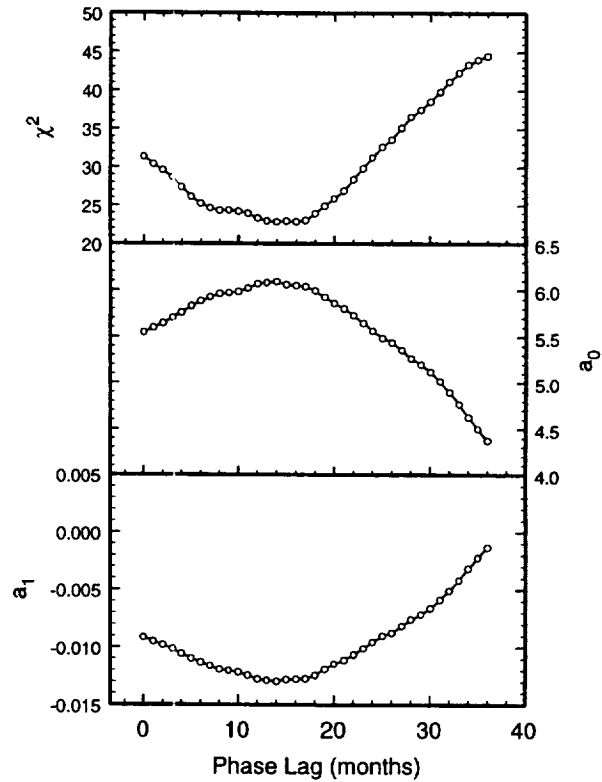


Figure 5-1. Variation of χ^2 , a_0 , and a_1 with assumed phase lag for a typical point in ζ - L' space.

In developing the model we chose to model the count rate for each channel, not the particle flux corresponding to the channel energy range. Once the count rates are modeled, the flux can be easily determined. This approach was necessary because of the nature of the MEPED omnidirectional data. The P6 and P7 channels contain two separate responses: the primary response for the channel's energy, and the response of the P8 channel, which must be subtracted from the total response. In practice, the P6 and P7 count rates at a given time point are often dominated by the P8 response, and often lie within the statistical uncertainty of the P8 channel. The P7 channel, in particular, often has instantaneous count rates which are actually lower than those of the P8 channel at the same time. The data smoothing process described earlier combines many data points and effectively decreases the statistical uncertainty. Thus, in the smoothed 10-day averages, we see P6 and P7 count rates which are consistently higher than P8.

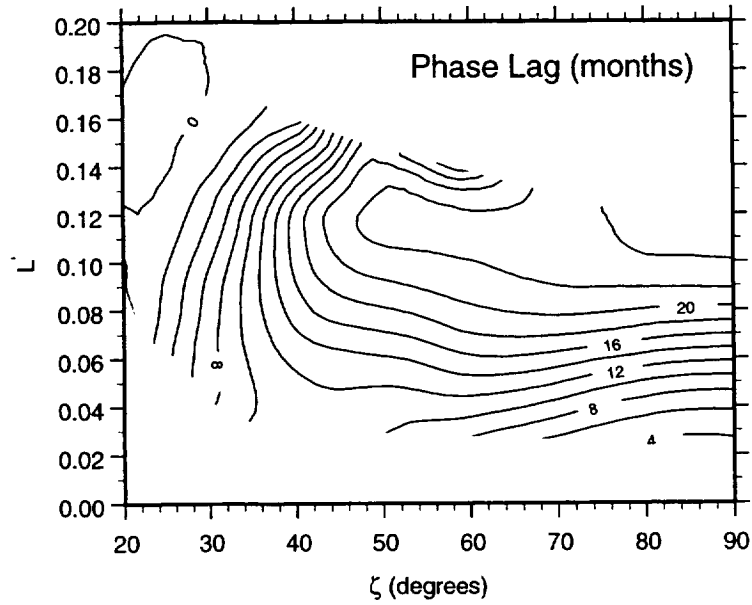


Figure 5-2. Isocontours of phase lag in ζ - L' space for the P8 channel.

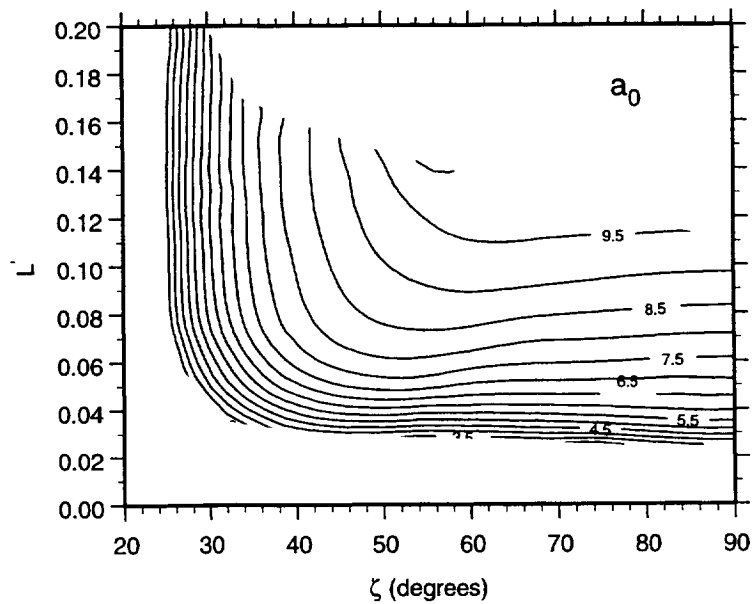


Figure 5-3. Isocontours of a in ζ - L' space for the P8 channel.

5.2 Model Implementation

We have implemented the model in the form of a set FORTRAN subroutines which can be called from a user program, along with a set of data files which the subroutines read. In the past, we have found this approach to be the most convenient for the user, since his needs vary quite widely.

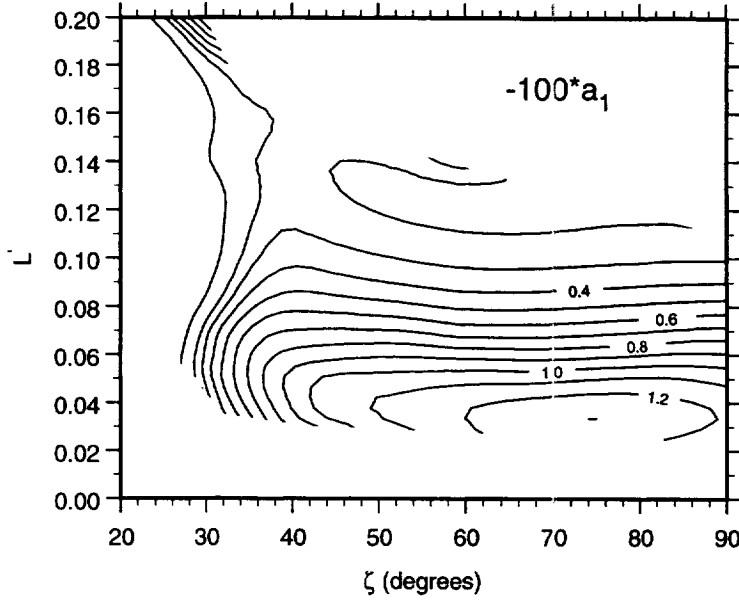


Figure 5-4. Isocontours of a_1 in ζ - L' space for the P8 channel.

SUBROUTINE NOAAPRO is called with the parameters DATE, B_{MIN}, XL, and FLUX. DATE is the decimal date, B_{MIN} is B/B_{\min} , and XL is the L -value in Earth radii for the point desired. B/B_{\min} and L *must* be determined using the magnetic field model appropriate for the epoch of interest. We recommend the INVARM subroutines and the routines it calls, as described in Reference 15; these routines are included with the NOAAPRO package. FLUX is the return value, a three-element array containing the omnidirectional integral proton flux in particles/cm²-sec for the three energy ranges: >16, >36, and >80 MeV.

Note that, although the model grid is in ζ - L' space, the user still inputs the traditional B/B_{\min} and L . Conversion to the model coordinate system is done within the model.

The first time it is called, the subroutine reads in the two data tables. The first of these, called F107.DAT, contains the 13-month smoothed solar $F_{10.7}$ flux as a function of time. The flux must be available for at least 24 months before the time point of interest. The second data file, called NOAAPRO.DAT, contains the parameters τ , a_0 , and a_1 as functions of B/B_{\min} and L .

Once the data files have been read in, the subroutine determines the proton flux by interpolating in the data tables to find the appropriate values of τ , a_0 , and a_1 for the input B/B_{\min} and L . From the interpolated value of τ , the subroutine then determines the value of $F'_{10.7}$, the phase-shifted solar radio flux. The count rate C_i for the i th channel is then determined by the relation

$$C_i = \exp(a_{0,i} + a_{1,i} F'_{10.7})$$

Once the count rates are determined, the P8 response is subtracted from the P6 and P7 count rates, and the count rates are converted to flux:

$$F_i = C_i / f_{g,i} ; i = P8.$$

$$F_i = F_{P8} + (C_i - C_{P8}) / f_{g,i} ; i = P6, P7,$$

where $f_{g,i}$ is the geometric factor for each channel. This approach preserves the maximum amount of data available in the smoothed data set. If new information becomes available on the relationships among the detectors, electron contamination, or changes in detector efficiencies, simple changes to the final algorithm can be used to correct the final flux calculated.

5.3 Model Results

Figures 5-5 through 5-8 compare the count rates predicted by the model with the actual measured count rates. The symbols show the actual data, and the solid lines show the flux determined from the model. The model follows the data quite well, particularly in terms of the minima and maxima. There are some discrepancies during the rising and falling portions of the solar cycle. In particular, the model flux does not decrease as quickly as the data show. This behavior may be due to the fact that our model is based only on a phase-shifted value of $F_{10.7}$. This fact amounts to an implicit assumption that the strengths of the source and loss processes are equal and produce similar phase lags during the rising and falling parts of the cycle. Also, we have data from two periods when the flux is increasing (1982–87 and 1992–present) and only one full period when the flux is decreasing (1988–90). Thus the model is somewhat biased towards the periods of increasing flux. The model errors are greater at smaller ζ , due mainly to the larger data scatter in this region.

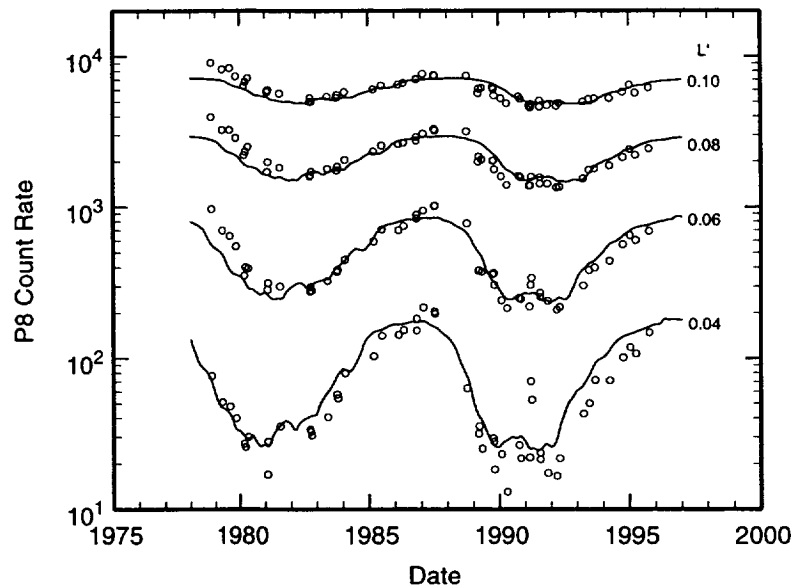


Figure 5-5. Comparison of the P8 count rate predicted by the NOAA PRO model with actual data at the geomagnetic equator ($\zeta=90^\circ$).

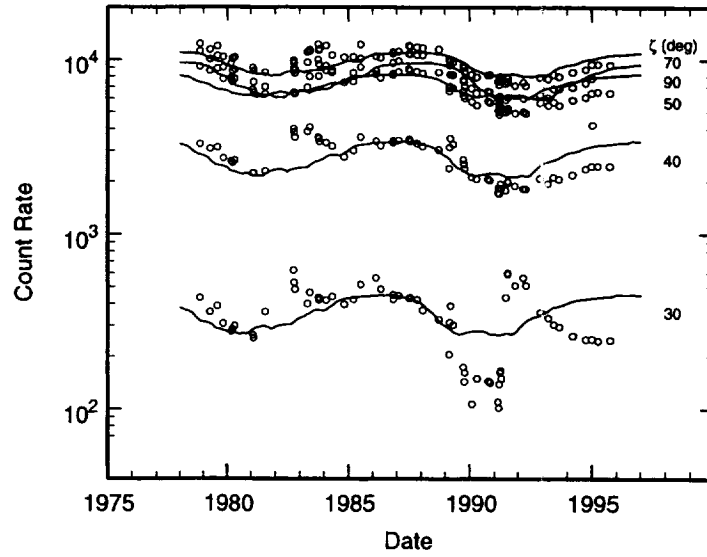


Figure 5-6. Comparison of the P6 count rate predicted by NOAAAPRO with measured data at $L'=0.10$.

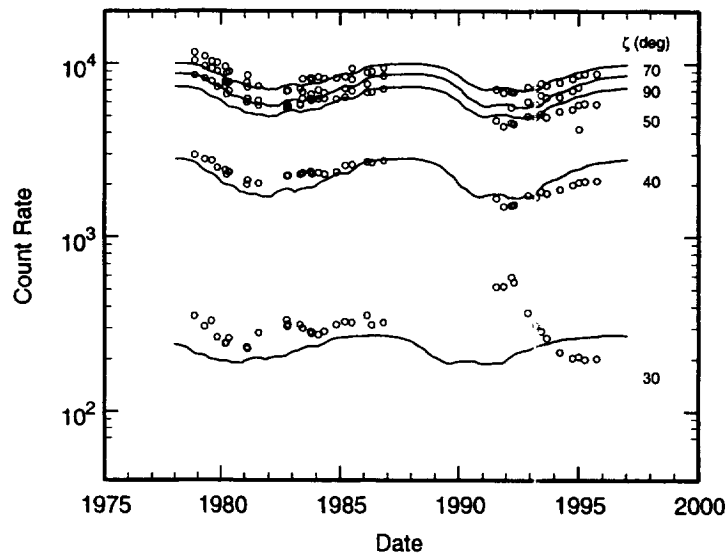


Figure 5-7. Comparison of the P7 count rate predicted by NOAAAPRO with measured data at $L'=0.10$.

Also note the large event which occurred between 1989 and 1994 at around $\zeta=30^\circ$. The count rate in all three channels decreases abruptly in 1989 (apparently related to the large solar events that year) and then stays lower than expected through 1990. In 1991, the flux increases suddenly (apparently related to the March 1991 event), then decays slowly back to around the expected value. The event is seen in all three channels. Even though these data were included in the model development process, the model does not reproduce this behavior because it is rather localized in ζ - L' space.

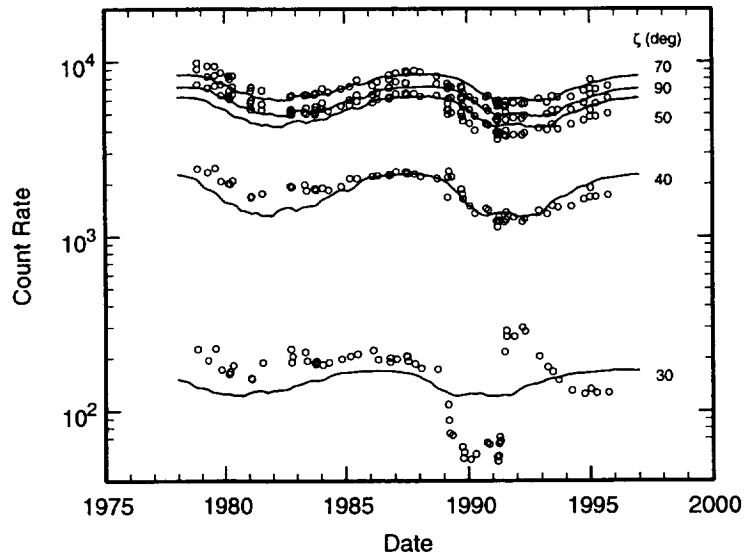


Figure 5-8. Comparison of the P8 count rate predicted by NOAA PRO with measured data at $L'=0.10$

Figure 5-9 shows a scatter plot of the predicted count rate vs. the actual count rate for the P8 channel over the entire ζ - L' space and over the entire time period. The model tends to overpredict the count rate at low count rates. This behavior is primarily due to the fact that the data smoothing and curve fitting procedures tend to minimize the variance over the entire dynamic range of the data, thus effectively giving more weight to the large values. A process which applies a weighting factor inversely proportional to the data value would probably result in better predictions when the count rate is low. There is also a significant population of points where the model significantly underpredicts the data. These points correspond to the solar proton events previously noted.

Figure 5-10 shows the probability of obtaining a given accuracy with the model. Overall, about 80% of the predictions lie within 50% of the data, and approximately 90% of the predictions are within a factor of 2 of the data (*i.e.*, the error is less than 100%). The median error is approximately 20%.

5.4 NOAA-10 P7 Channel

As discussed in Section 4, the P7 channel on NOAA-10 produced anomalous results. This was unfortunate because NOAA-10 provided 27 of the 67 data files used in the modeling process. NOAA-10 also provided the only data around the proton flux maximum in the 1986 – 1988 period.

We initially attempted to build a model for the P7 channel simply by excluding the NOAA-10 data. This approach produced a model in which the phase lags and solar cycle dependence for

the P7 channel were quite different from those of P6 and P8. We felt that this model was inadequate and investigated procedures for compensating for the lack of NOAA-10 data.

We chose a relatively simple approach in which we generated a set of pseudo-data for the NOAA-10 P7 channel to substitute for the anomalous data. We first analyzed all the data for the other spacecraft. In looking at the logarithm of the count rate for the three channels, the ratio of the difference between P7 and P8 to the difference between P6 and P8 was relatively constant, within a broad range; *i.e.*:

$$\frac{[\ln(P7) - \ln(P8)]}{[\ln(P6) - \ln(P8)]} \approx 0.591$$

We therefore generated a pseudo-data set in which the P7 channel count rate is determined from the above relation. The model parameters for the P7 channel were determined using this pseudo-data set.

While this procedure was very simple, the results were quite good. The goodness-of-fit statistics discussed in the previous subsection (Figure 5-10) **do not** include the pseudo-data. They compare the model prediction with the actual data from the spacecraft other than NOAA-10. The agreement between the model and the data is actually better for the P7 channel than for P6. The ultimate test of the model is how well it agrees with the actual data, and using our procedure the model works quite well.

5.5 Comparison with AP8

Section 4.5 compared the >80 MeV flux measured by the MEPED with AP8 in B/B_{\min} - L space. While this comparison is good for showing the details of the differences between the data and the AP8 model, it is difficult to get an overall idea of the differences between the two.

Because AP8 is tied to specific magnetic field models, it cannot be used to compare with other models in geographic space. We have therefore performed an orbital integration for circular polar orbits of various altitudes and compared the integrated fluence predicted by AP8 and NOAAPRO. Figures 5-11 and 5-12 show the ratio of the fluence predicted by NOAAPRO to that predicted by AP8, for both solar minimum and solar maximum. For all three energies and both levels of solar activity, NOAAPRO consistently predicts fluxes a factor of about 1.8–2.4 higher than AP8.

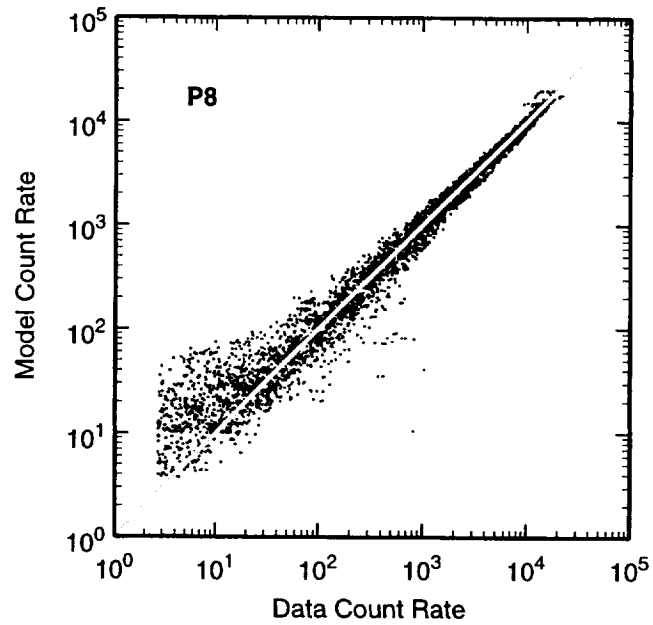


Figure 5-9. Scatter plot showing the P8 count rate predicted by NOAAAPRO vs. the actual measured count rate, for the entire data set used to develop the model. The gray diagonal line indicates a perfect correlation.

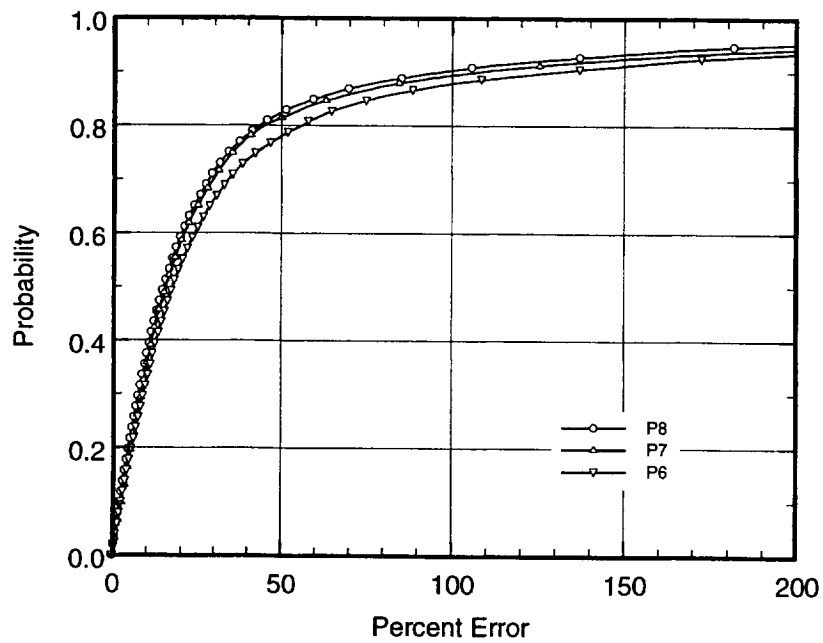


Figure 5-10. Probability of obtaining a given percent error using the NOAAAPRO model.

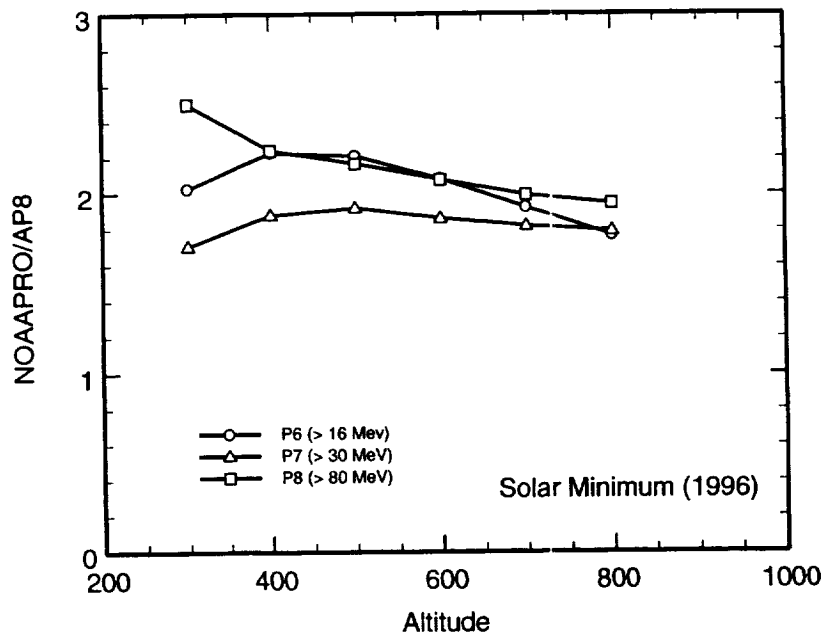


Figure 5-11. Ratio of fluence predicted by NOAAPRO to that predicted by AP8 for circular polar orbits of various altitudes at solar minimum conditions.

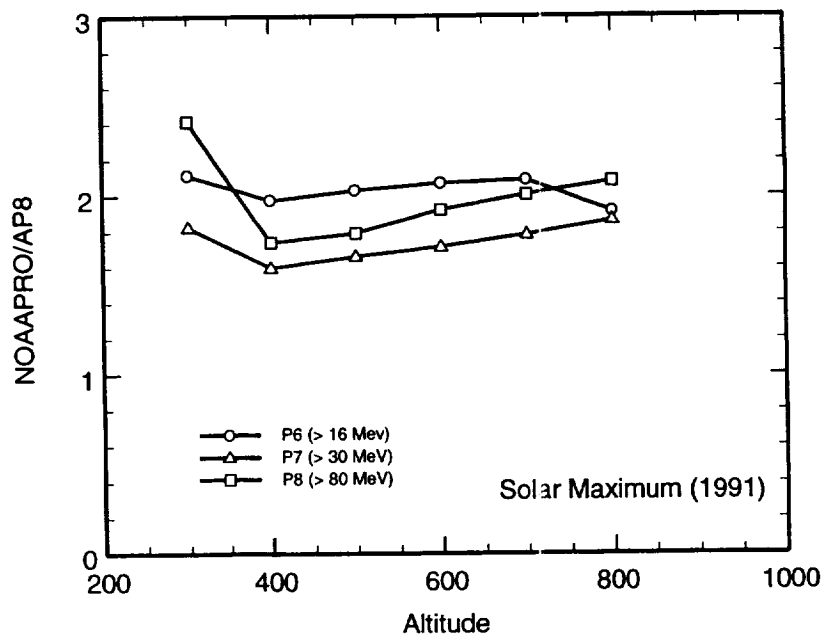


Figure 5-12. Ratio of fluence predicted by NOAAPRO to that predicted by AP8 for circular polar orbits of various altitudes at solar maximum conditions.

6. SUMMARY AND CONCLUSIONS

The model and data base developed under this study represent a major advancement in our ability to understand and predict the trapped radiation environment.

6.1 NOAAPRO Model

The NOAAPRO model provides the first true solar cycle dependence for trapped proton models. It provides better spatial resolution at low altitudes, where solar activity affects the trapped radiation flux. The model also correctly accounts for the secular change in the Earth's magnetic field, and thus allows the model to be used to predict the proton flux at a given location in geographic space. The model is valid for essentially the entire region where atmospheric effects are important.

We have performed an extensive analysis of the characteristics of the MEPED instruments and the accuracy of the model. Overall, the median error of the model is only about 20%, and the model provides predictions within 50% of measured data approximately 80% of the time. This accuracy greatly exceeds the accuracy available with previous models. The major uncertainty in the model is the potential for electron contamination in the P6 channel. There is simply not enough data available under this study to fully resolve this issue.

The model addresses most of the issues regarding AP8, but at present it cannot be considered a replacement for AP8. The model is only valid up to altitudes of about 850 km, since it is based entirely on data from this region. The energy range and resolution of the model are also limited.

Despite these drawbacks, the model has many engineering and scientific uses. It can provide an idea of how accurate (or inaccurate) AP8 is. The model is especially useful in providing predictions for operations in which geographic accuracy is required (such as EVA or sensitive measurements). In fact, a preliminary version of the model has already been used to investigate single-event upsets on several low-altitude spacecraft. The model also has many scientific uses, particularly studying source and loss mechanisms in the inner zone.

6.2 MEPED Data Base

The MEPED data base, including data from the particle telescopes which was not used in this study, is also a significant resource to the scientific and engineering community. We have greatly improved the usefulness of this data base by re-processing the data to include more accurate magnetic coordinates. The data base has many potential uses, including modeling the electron environment and investigating low-energy protons.

6.3 Future Efforts

The NOAAAPRO model provides an excellent basis for developing a new model which can replace AP8. NASA is currently planning a further effort under the SEE program to combine the NOAAAPRO model with data from CRRES and other spacecraft to obtain a model which will cover the entire spectral and spatial region of interest. This effort should be complemented by similar efforts in Europe, Russia, and Japan.

This effort will also provide the opportunity to correct some outstanding issues with NOAAAPRO. We have not fully resolved the issue of electron contamination in the P6 channel; the follow-on study will require extensive cross-calibration of the MEPED data with other spacecraft, thus providing a much better idea of the magnitude of the effect. There is also much more data available since October 1995, the last data used in this study. Including this newer data would provide more data at solar minimum and in the rising portion of solar activity, and could also compensate for the lack of P7 data at solar minimum (due to the anomaly on the NOAA-10 spacecraft).

In addition, while the MEPED data base is extremely useful, it is actually rather limited. It contains only about 670 days of data out of more than 7500 days available in the entire TIROS/NOAA data base. These data are available from NGDC, and the entire data base could be reprocessed at minimal cost to the government. In addition, the RDCOR program we wrote to access the data base is not particularly user-friendly and could be re-written to provide easier access to the data. It would also be useful to reformat the data using NASA's Common Data Format (CDF), which provides a standard interface.

7. REFERENCES

- 1) Vette, J. I., The NASA/National Space Science Data Center Trapped Radiation Environment Program (1964-1991), NSSDC/WDC-A 91-29, November 1991.
- 2) Konradi, A., A. C. Hardy, and W. Atwell, "Radiation Environment Models and the Atmospheric Cutoff," *J. Spacecraft*, 24, 284-285, 1987.
- 3) Heyderickx, D., "Comparison Between Methods to Compensate for the Secular Motion of the South Atlantic Anomaly," *Radiation Measurements*, 26, pp. 369-373, 1996.
- 4) Huston, S. L., G. A. Kuck, and K. A. Pfitzer, Low altitude trapped radiation model using TIROS/NOAA data, *Radiation Belts: Models and Standards*, AGU Geophysical Monograph 97 (1996)
- 5) Armstrong, T. W., et al., Comparison of model predictions with LDEF satellite radiation measurements, *Adv. Space Res.*, 14, 17 (1994)
- 6) Badhwar, G. D., A. Konradi, L. A. Braby, W. Atwell, and F. A. Cucinotta, Measurements of trapped protons and cosmic rays from recent shuttle flights, *Adv. Space Res.*, 14, 67 (1994)
- 7) Vampola, A. L., M. Lauriente, S. Huston, and K. Pfitzer, Validating the new SEE low altitude proton model, presented at IEEE Conference on the High Energy Radiation Background in Space (CHERBS), Snowmass, CO, July 23-24, 1997, to be published. Also available electronically at <http://envnet.gsfc.nasa.gov/Papers/SEELAPM.html>.
- 8) Seale, R. A. and R. H. Bushnell, The TIROS-N/NOAA A-J Space Environment Monitor Subsystem, NOAA Technical Memorandum ERL SEL-75, NOAA Space Environment Laboratory, Boulder, Colorado, April 1987.
- 9) Hill, V. J., D. S. Evans, and H. H. Sauer, TIROS/NOAA Satellites Space Environment Monitor Archive Tape Documentation, NOAA Technical Memorandum ERL SEL-71, NOAA Space Environment Laboratory, Boulder, Colorado, January 1985.
- 10) Raben, V. J., D. S. Evans, H. H. Sauer, S. R. Sahm, and M. Huynh, TIROS/NOAA Satellite Space Environment Monitor Data Archive Documentation: 1995 Update, NOAA Technical Memorandum ERL SEL-86, NOAA Space Environment Laboratory, Boulder, Colorado, February 1995.
- 11) Stassinopoulous, E. G., and G. D. Mead, ALLMAG, GDALNG, LINTRA: Computer Programs for Geomagnetic Field and Field-Line Calculations, NASA/NSSDC Report 72-12.
- 12) Abel, B., R. M. Thorne, and A. L. Vampola, Solar cyclic behavior of trapped energetic electrons in Earth's inner radiation belt, *J. Geophys. Res.* 99, 19,427 (1994).
- 13) Wilson, J. W., et al., BRYNTRN: A Baryon Transport Model, NASA TP 2887, March 1989.

- 14) Hoots, F. R., and R. L. Roehrich, Spacetrack Report No. 3: Models for Propagation of NORAD Element Sets, available on World Wide Web at URL <http://www.grove.net/~tkelso/NORAD/documentation/spacetrk.pdf> or <ftp://archive.afit.af.mil/pub/space/spacetrk.pdf>, December 1988.
- 15) Pfitzer, K. A., Improved Models of the Inner and Outer Radiation Belts, Phillips Laboratory Final Report, PL-TR-96-2050, December 1995.
- 16) Barraclough, D. R., International Geomagnetic Reference Field: the fourth generation, *Phys. Earth Planet. Inter.*, **48**, 279 (1987)
- 17) Hilton, H. H., L parameter, a new approximation, *J. Geophys. Res.* **76**, 6952-6955 (1971)
- 18) McIlwain, C. E., Coordinates for mapping the distribution of magnetically trapped particles, *J. Geophys. Res.*, **66**, 3681-3691, 1961.
- 19) Cleveland, W. S., and E. Grosse, Computational methods for local regression, *Statistics and Computing*, **1**, 47 (1991) (also see document published electronically as <http://www.netlib.org/a/cloess.ps>)
- 20) Blanchard, R. C., and W. N. Hess, Solar cycle changes in inner zone protons, *J. Geophys. Res.*, **69**, 3927 (1964)
- 21) Pfitzer, K. A., Radiation dose to man and hardware as a function of atmospheric density on the 28.5° space station orbit, McDonnell Douglas Space Systems Co. Report No. H5387A, Huntington Beach, CA (1990)
- 22) Lemaire, J., A. D. Johnstone, D. Heynderickx, D. J. Rodgers, S. Sitz, and V. Pierrard, Trapped radiation environment model development TREND-2 Final Report, *Aeronomica Acta A* No. 393-1995 (1995)
- 23) Press, W. H., B. P. Flannery, S. A. Teukolsky, and W. T. Vetterling, *Numerical Recipes*, Cambridge University Press, Cambridge, 1986.

Appendix A

TIROS/NOAA Data Set

Table A-1 lists the individual TIROS/NOAA data files used to develop the NOAAAPRO model. These files have been processed by Boeing and contain the corrected *B/L* coordinates. The table lists the file name, the spacecraft, the data start date (most files contain either 10 or 11 days of data), the value of the 13-month smoothed solar 10.7 cm radio flux ($F_{10.7}$) for that month, and the recommended time shift (see the discussion in Section 3.2 of the report). These files can be read using the RDCOR.EXE program.

Table A-1. TIROS/NOAA data files used during model development.

File Name	S/C	Start Date	$F_{10.7}$	Time Shift (sec)	Comments
TN8306.COR	TIROS-N	2-Nov-78	162.5	0	Start of data
TN9101.COR	TIROS-N	11-Apr-79	171.3	-8	
N69213.COR	NOAA-06	1-Aug-79	186.2	0	
TN9305.COR	TIROS-N	1-Nov-79	195.7	-8	
TN0061.COR	TIROS-N	1-Mar-80	194.6	0	TIROS-N/NOAA-06
N60081.COR	NOAA-06	21-Mar-80	194.6	0	TIROS-N/NOAA-06
N60122.COR	NOAA-06	1-May-80	201.9	8	
N61032.COR	NOAA-06	1-Feb-81	183.3	-8	
TN1042.COR	TIROS-N	11-Feb-81	183.3	0	
N61213.COR	NOAA-06	1-Aug-81	178.7	8	
N62274.COR	NOAA-06	1-Oct-82	156.9	-8	
N62284.COR	NOAA-06	11-Oct-82	156.9	-16	
N62294.COR	NOAA-06	21-Oct-82	156.9	-8	
N63121.COR	NOAA-06	1-May-83	133.6	-8	
N83152.COR	NOAA-08	1-Jun-83	127.7	-8	
N83274.COR	NOAA-08	1-Oct-83	124.2	-8	
N83284.COR	NOAA-08	11-Oct-83	124.2	-16	
N83294.COR	NOAA-08	21-Oct-83	124.2	-8	
N84032.COR	NOAA-08	1-Feb-84	117.5	-16	
N84122.COR	NOAA-08	1-May-84	103.1	0	
N64306.COR	NOAA-06	1-Nov-84	83.4	-16	
N65070.COR	NOAA-06	11-Mar-85	81.1	-16	
N85182.COR	NOAA-08	1-Jul-85	77.1	-16	

Table A-1. TIROS/NOAA data files used during model development.
(Continued)

File Name	S/C	Start Date	F _{10.7}	Time Shift (sec)	Comments
N66052.COR	NOAA-06	21-Feb-86	75.0	0	
N66121.COR	NOAA-06	1-May-86	74.8	0	
N66305.COR	NOAA-06	1-Nov-86	74.9	-8	NOAA-06/NOAA-10
N06305.COR	NOAA-10	1-Nov-86	74.9	-8	NOAA-06/NOAA-10
N07032.COR	NOAA-10	1-Feb-87	78.9	-8	
N07182.COR	NOAA-10	1-Jul-87	86.8	0	
N07192.COR	NOAA-10	11-Jul-87	86.8	0	
N07202.COR	NOAA-10	21-Jul-87	86.8	-8	
N07305.COR	NOAA-10	1-Nov-87	98.6	8	
N08032.COR	NOAA-10	1-Feb-88	114.6	8	
N08275.COR	NOAA-10	1-Oct-88	169.5	0	
N09060.COR	NOAA-10	1-Mar-89	191.3	0	March '89 events
N09070.COR	NOAA-10	11-Mar-89	191.3	0	March '89 events
N09080.COR	NOAA-10	21-Mar-89	191.3	8	March '89 events
N09121.COR	NOAA-10	1-May-89	198.2	-16	
N09274.COR	NOAA-10	1-Oct-89	197.4	8	Oct. '89 events
N09284.COR	NOAA-10	11-Oct-89	197.4	0	Oct. '89 events
N09294.COR	NOAA-10	21-Oct-89	197.4	-8	Oct. '89 events
N00032.COR	NOAA-10	1-Feb-90	191.9	-8	
N00111.COR	NOAA-10	21-Apr-90	194.6	-8	RME III / STS-31
N00274.COR	NOAA-10	1-Oct-90	205.7	-16	RME III / STS-41
N00305.COR	NOAA-10	1-Nov-90	204.9	-8	
N01060.COR	NOAA-10	1-Mar-91	208.1	-8	CRRES Event
N01070.COR	NOAA-10	11-Mar-91	208.1	0	CRRES Event
N01080.COR	NOAA-10	21-Mar-91	208.1	0	CRRES Event
N01091.COR	NOAA-10	1-Apr-91	204.4	-8	RME II / STS-37
N01101.COR	NOAA-10	11-Apr-91	204.4	0	CRRES Event
N01111.COR	NOAA-10	21-Apr-91	204.4	-16	RME III / STS-39
N01182.COR	NOAA-10	1-Jul-91	201.3	0	
N01213.COR	NOAA-10	1-Aug-91	202.7	-8	NOAA-10/NOAA-12
N21213.COR	NOAA-12	1-Aug-91	202.7	-8	NOAA-10/NOAA-12
N21325.COR	NOAA-12	21-Nov-91	195.0	-8	RME III / STS-44
N22081.COR	NOAA-12	21-Mar-92	164.1	-8	RME III / STS-45
N22122.COR	NOAA-12	1-May-92	153.6	-8	

*Table A-1. TIROS/NOAA data files used during model development.
(Continued)*

File Name	S/C	Start Date	F _{10.7}	Time Shift (sec)	Comments
N22336.COR	NOAA-12	1-Dec-92	135.6	-8	RME III / STS-53
N23091.COR	NOAA-12	1-Apr-93	118.4	0	RME III / STS-56
N23172.COR	NOAA-12	21-Jun-93	112.6	-8	CPDS / STS-57
N23254.COR	NOAA-12	11-Sep-93	109.1	-8	RME III / STS-51
N24091.COR	NOAA-12	1-Apr-94	90.6	0	
N24274.COR	NOAA-12	1-Oct-94	85.8	0	
N25001.COR	NOAA-12	1-Jan-95	80.6	-8	NOAA-12/NOAA-14
N45011.COR	NOAA-14	11-Jan-95	80.6	-16	NOAA-12/NOAA-14
N25091.COR	NOAA-12	1-Apr-95	79.2	-8	
N25274.COR	NOAA-12	1-Oct-95	73.8	-8	

Appendix B

NOAAPRO Model

The NOAAPRO model determines the omnidirectional integral proton flux for three energies (>16 , >30 , >80 MeV) as a function of the solar activity as expressed by the 10.7 cm solar radio flux ($F_{10.7}$). In order to provide the greatest flexibility for both scientific and engineering users, the model is supplied in the form of source code subroutines which can be called from the user's own main program. The model actually consists of three parts: the data files themselves, a set of subroutines which read the data files and determine the proton flux at a given point in B/L space, and a set of subroutines which calculate B/L coordinates at a point in geographic space. This document describes the files which make up the model and provides instructions for calling the subroutines.

PROGRAM FILES

The model is currently provided in FORTRAN source code form. The user should provide a main program which calls the NOAAPRO subroutines, along with performing whatever input/output (I/O) functions the user desires. The user should compile and link the main program and the NOAAPRO routines; the code should be consistent with any modern compiler.

In order to demonstrate the use of the model, we have provided two sample main programs which perform functions for which the model might commonly be used. The following table describes the program files in the NOAAPRO distribution.

File Name	Description
NOAAPRO.FOR	The source code for the NOAAPRO model. The main subroutines are called NOAAPRO, which determines the proton flux, and GETB, which determines the magnetic field parameters. The calling parameters for these subroutines are described below.
NOAABL.FOR	Source code for the main program which determines the proton flux at a given altitude on a grid of longitude/latitude points. The main program must be linked with the subroutines in NOAAPRO.FOR and CRRESBL.FOR.
NOAABL.EXE	The executable version of the above program (linked with the appropriate subroutines). This version should run on any 486 or higher PC with Win32S.
NOAABL.OUT	Sample output from NOAABL.EXE.
NOAAEPH.FOR	The source code for the main program which reads an ephemeris file and calculates the proton flux and fluence for an orbit. The main program must be linked with the subroutines in NOAAPRO.FOR and CRRESBL.FOR. The file EPHEM.TXT is a sample ephemeris file.
NOAAEPH.EXE	The executable version of the above program (linked with the appropriate subroutines). This version should run on any 486 or higher PC with Win32S.

EPHEM.TXT	A sample ephemeris file for use with the NOAAEPH.EXE program. This is actually an output file from Al Vampola's RADMODLS program. It contains altitude, latitude, and longitude as a function of time for an 800km, 90 degree inclination orbit. It also contains the AP8 predicted flux for the three NOAA channels.
NOAAEPH.OUT	Sample output from NOAABL.EXE (with EPHEM.TXT as input).
CRRESBL.FOR	The subroutines for the CRRES B/L computations

DATA FILES

The main data file is called NOAAPRO.DAT, and contains the curve fit parameters necessary for determining the proton flux for each energy range. For more information on these parameters and the format of the file, please see the final report.

Since the NOAAPRO model depends on the solar $F_{10.7}$ flux, we have supplied a separate data file containing $F_{10.7}$ as a function of time. From 1960 through 1997, the file contains the actual 13-month smoothed value of $F_{10.7}$. Since the NOAAPRO model may be used to predict the proton flux for future dates, we have also included predicted $F_{10.7}$ values for the period 1998 – 2005. Since such predictions are highly uncertain, we have included predictions for “high”, “nominal”, and “low” predictions for Cycle 23. These predictions are based on conferences held in September 1996 and September 1997, in which a panel of experts discussed various methods for predicting solar activity for Solar Cycle 23. The findings of this panel can be found on the World Wide Web at URL <http://www.sec.noaa.gov/info/Cycle23.html>. We have also included a file which takes the $F_{10.7}$ history for Cycle 20 and assumes Cycle 23 will follow the same history; this would be tantamount to assuming a historically low level of solar activity. The data file read by NOAAPRO *must* be named F107.DAT; thus, if the user wishes to assume a different solar activity model than the “nominal” value, he should copy one of the other files to F107.DAT.

File Name	Description
NOAAPRO.DAT	The data file making up the NOAAPRO model.
F107.DAT	Contains the “nominal” $F_{10.7}$ for Cycle 23 (same as F107NOM.DAT)
F107HI.DAT	Contains the highest expected $F_{10.7}$ for Cycle 23. The maximum value is 235.3.
F107LO.DAT	Contains the lowest expected $F_{10.7}$ for Cycle 23. The maximum value is 175.
F107NOM.DAT	Contains the nominal expected $F_{10.7}$ for Cycle 23. The maximum value is 205.
F107C20.DAT	Contains the $F_{10.7}$ history from Cycle 20 projected for Cycle 23. The maximum value is 153.8. This can be taken as an absolute minimum expected value for $F_{10.7}$.
F107ALL.DAT	Contains all 4 $F_{10.7}$ predictions for Cycle 23.

DESCRIPTIONS OF SUBROUTINES

The two main programs, NOAABL.FOR and NOAAEPH.FOR, demonstrate the use of the magnetic field and proton flux subroutines. The following tables give details of the calling parameters for these subroutines.

SUBROUTINE NOAAPRO

Subroutine NOAAPRO determines the omnidirectional integral proton flux for each of the MEPED energy bands (>16, >30, >80 MeV) in protons/cm²/sec.

Parameter	Type	Description/Notes
<i>Inputs:</i>		
DATE	REAL*4	The decimal date in yyyy.yyyy format. For example, 1 June 1991 would be 1991.416.
BBMIN	REAL*4	B/B _{min}
XL	REAL*4	L (in Earth radii) NOTE: BBMIN and XL MUST be determined using an internal magnetic field model appropriate to the epoch of interest.
<i>Outputs:</i>		
FLUX(3)	REAL*4	Omnidirectional proton flux in protons/cm ² /sec. FLUX(1) is the P6 channel (>16 MeV) FLUX(2) is the P7 channel (>30 MeV) FLUX(3) is the P8 channel (>80 MeV) If the value returned for FLUX is negative, an error condition has occurred. FLUX=-1.0 --> outside the region of validity FLUX=-2.0 --> there weren't enough points to interpolate FLUX=-3.0 --> went beyond the bounds of the $F_{10.7}$ file

SUBROUTINE GETB

The input parameters BBMIN and XL ***MUST*** be determined using the CRRES B/L model. They can be determined by calling SUBROUTINE GETB, using the parameters listed below.

Parameter	Type	Description/Notes
<i>Inputs:</i>		
XLAT	REAL*4	Geographic latitude (degrees East)
XLONG	REAL*4	Geographic longitude (degrees North)
RAD	REAL*4	Geographic radius (km)

YR	REAL*4	Year (yyyy format). For example, 1 June 1991 would be 1991.416. ***NOTE*** YR should be changed only every few days or months. New field coefficients must be computed for every change in YR, and this could cause a large increase in computer time. The Earth's field changes only about .001 gauss/year at the Earth's surface. If YR is changed by more than .1 year new field coefficients are computed.
DAY	REAL*4	Day of year
TIME	REAL*4	Time of day (hours)
<i>Outputs:</i>		
EL	REAL*4	L value (Re)
BLOCAL	REAL*4	Local value of B-field (nT)
BR	REAL*4	Radial component of B-field (nT)
BP	REAL*4	E component of B-field (nT)
BT	REAL*4	S component of B-field (nT)
BMIN	REAL*4	Minimum value of B along field line

Any questions or comments should be directed to:

Mr. Stuart L. Huston
The Boeing Company
5301 Bolsa Avenue
Huntington Beach, CA 92647
USA
Phone: 714-896-4787
Fax: 714-896-4587
e-mail: STUART.L.HUSTON@BOEING.COM

Appendix C

Corrected MEPED Data Base

We are supplying the entire data base of corrected MEPED data used to develop the NOAAAPRO model on CD-ROM. This data base consists of the 8-second averaged data from the MEPED instrument, with the corrected B/L coordinates calculated with the CRRES B/L routine. These data are in packed binary format and must be extracted with a program that can read the files. We are supplying the RDCOR.C program which we used to extract the data for analysis. This document briefly describes the program and the structure of the data files.

RDCOR.C

RDCOR.C is a relatively simple C program which reads the packed binary data, unpacks it, converts it to engineering units, and outputs the data to an ASCII file.

The heart of the program is the C structure used to write and read each record of data; this structure is called *nMEPED* and is described in the C header file *NMEPED.H*. Table C-1 summarizes this structure. All data are stored as integers. The 'word' data type is an unsigned two-byte integer, and the 'byte' data type is an unsigned one-byte integer. In the table, the column labeled "Factor" gives the conversion factor used to convert decimal values to integers. This information is necessary to

Table C-1. Elements of the nMEPED data structure

Type	Name	Description	Unit	Factor	Byte Ct.
word	ID	Spacecraft ID			1-2
word	year	Year (0-99)			3-4
word	day	Day of the year			5-6
long	msec	Milliseconds of the day			7-10
short	slat	Geographic north latitude	deg	.01	11-12
word	slon	Geographic east longitude	deg	.01	13-14
word	salt	Altitude	km	.1	15-16
short	BR	Radial comp. of B-field	nT	2	17-18
short	BT	N/S comp. of B-field	nT	2	19-20
short	BP	E/W comp. of B-field	nT	2	21-22
short	BMIN	Bmin on field line	nT	2	23-24
word	L	L-value (0.0 if L > 14.99)	Re	.01	25-26
word	MP81	MEPED 83 deg pitch angle	deg	.01	27-28
word	MP0	MEPED 0 deg pitch angle	deg	.01	29-30
byte	counts[19]	Packed counts for the 19 channels		–	31-49
byte	dummy[7]	dummy fill			50-56

unpack the data. For example, to convert the variable slat to the latitude, the value of slat must be multiplied by 0.01.

Input/Output

RDCOR.C performs these conversions for each record in the corrected data file. It extracts records which conform to a set of user-specified criteria, and writes data to an ASCII file. The selection criteria and data to write are provided in a user-generated input file.

Table C-2 lists the quantities available for the output and selection criteria.

The input file contains four lines. The first three lines specify the selection criteria, and each line should contain the three values: the index number of the variable (from Table C-2), the minimum value for selection, and the maximum value for selection. Each value should be separated by blanks. The fourth line specifies the output values. The first number on the line is the n_{out} , the number of output values desired; this should be followed by n_{out} values indicating the output quantities desired. The following lines present an example.

```
6  1.0 1.0001
7  1.0 10.0
0  0.0 99.0
6  1 28 7 24 25 26
```

The first line tells the program to extract records with $1.0 \leq B/B_{min} \leq 1.0001$; the second line tells the program to extract points with $1.0 \leq L \leq 10.0$; and the third line tells the program to extract records with the day of year between 0 and 99 (obviously, this criterion will be met for all records). All the criteria must be met for a record to be extracted. Finally, the fourth line tells the program to output six values: the time of day, the parameter ζ , L , and the count rates for the P6, P7, and P8 channels.

RDCOR.C is run from the DOS command line. The format is:

```
rdcor datafile outfile_base_name noffset input_file
```

where:

datafile is the name of the corrected binary data file

outfile_base_name is the base name of the output file desired. An extension of .TXT will automatically be appended to the file name.

noffset is an integer indicating the amount of time offset to use. *noffset*=0 indicates a time offset of -16 seconds, *noffset*=1 indicates an offset of -8 seconds, and so on. Valid values are integers between 0 and 4.

input_file is the name of the input file.

The files DEMO.BAT and DEMO.INP provide examples of how to run RDCOR.

Table C-2.

Index	Variable	Value
0	day	Day of year
1	time	Time of day (seconds)
2	slat	Geographic North Latitude (degrees)
3	slon	Geographic East Longitude (degrees)
4	salt	Altitude (km)
5	Bmag	Magnetic field magnitude (Gauss)
6	BBmin	B/B_{min}
7	L	L-parameter (Earth radii)
8	P1_0	Count rate for the P1 channel of the 0-degree proton telescope (0P1; 30–80 keV)*
9	P2_0	Count rate for the 0P2 channel (80–250 keV)
10	P3_0	Count rate for the 0P3 channel (250–800 keV)
11	P4_0	Count rate for the 0P4 channel (800–2500 keV)
12	P5_0	Count rate for the 0P5 channel (>2500 keV)
13	E1_0	Count rate for the 0E1 channel (>30 keV)
14	E2_0	Count rate for the 0E2 channel (>100 keV)
15	E3_0	Count rate for the 0E3 channel (>300 keV)
16	P1_90	Count rate for the P1 channel of the 90-degree proton telescope (90P1; 30–80 keV)*
17	P2_90	Count rate for the 90P2 channel (80–250 keV)
18	P3_90	Count rate for the 90P3 channel (250–800 keV)
19	P4_90	Count rate for the 90P4 channel (800–2500 keV)
20	P5_90	Count rate for the 90P5 channel (>2500 keV)
21	E1_90	Count rate for the 90E1 channel (>30 keV)
22	E2_90	Count rate for the 90E2 channel (>100 keV)
23	E3_90	Count rate for the 90E3 channel (>300 keV)
24	P6	Count rate for the P6 omnidirectional channel (16–80 MeV)
25	P7	Count rate for the P7 omnidirectional channel (36–80 MeV)
26	P8	Count rate for the P8 omnidirectional channel (>80 MeV)
27		not used
28	zeta	Parameter ζ (degrees)

* all count rates are extracted as the natural logarithm of the count rate.

REPORT DOCUMENTATION PAGE			Form Approved OMB No. 0704-0188	
Public reporting burden for this collection of information is estimated to average 1 hour per response, including the time for reviewing instructions, searching existing data sources, gathering and maintaining the data needed, and completing and reviewing the collection of information. Send comments regarding this burden estimate or any other aspect of this collection of information, including suggestions for reducing this burden, to Washington Headquarters Services, Directorate for Information Operation and Reports, 1215 Jefferson Davis Highway, Suite 1204, Arlington, VA 22202-4302, and to the Office of Management and Budget, Paperwork Reduction Project (0704-0188), Washington, DC 20503				
1. AGENCY USE ONLY (Leave Blank)	2. REPORT DATE August 1998	3. REPORT TYPE AND DATES COVERED Contractor Report (Final)		
4. TITLE AND SUBTITLE Space Environment Effects: Low-Altitude Trapped Radiation Model		5. FUNDING NUMBERS		
6. AUTHORS S.L. Huston and K.A. Pfitzer				
7. PERFORMING ORGANIZATION NAME(S) AND ADDRESS(ES) The Boeing Company 5301 Bolsa Avenue Huntington Beach, CA 92647		8. PERFORMING ORGANIZATION REPORT NUMBER M-890		
9. SPONSORING/MONITORING AGENCY NAME(S) AND ADDRESS(ES) George C. Marshall Space Flight Center Marshall Space Flight Center, Alabama 35812		10. SPONSORING/MONITORING AGENCY REPORT NUMBER NASA/CR-1998-208593		
11. SUPPLEMENTARY NOTES Prepared for NASA's Space Environments and Effects (SEE) Program Technical Monitor: John Watts				
12a. DISTRIBUTION/AVAILABILITY STATEMENT Unclassified-Unlimited Subject Category 93 Standard Distribution		12b. DISTRIBUTION CODE		
13. ABSTRACT (Maximum 200 words) Accurate models of the Earth's trapped energetic proton environment are required for both piloted and robotic space missions. For piloted missions, the concern is mainly total dose to the astronauts, particularly in long-duration missions and during extravehicular activity (EVA). As astronomical and remote-sensing detectors become more sensitive, the proton flux can induce unwanted backgrounds in these instruments. Due to this unwanted background, the following description details the development of a new model for the low-trapped proton environment. The model is based on nearly 20 years of data from the TIRO/NOAA weather satellites. The model, which has been designated NOAAPRO (for NOAA protons), predicts the integral omnidirectional proton flux in three energy ranges: >16, >36, and >80 MeV. It contains a true solar cycle variation and accounts for the secular variation in the Earth's magnetic field. It also extends to lower values of the magnetic L parameter than does AP8. Thus, the model addresses the major shortcomings of AP8.				
14. SUBJECT TERMS ionizing radiation, radiation environment, space radiation, radiation		15. NUMBER OF PAGES 63		
		16. PRICE CODE A04		
17. SECURITY CLASSIFICATION OF REPORT Unclassified	18. SECURITY CLASSIFICATION OF THIS PAGE Unclassified	19. SECURITY CLASSIFICATION OF ABSTRACT Unclassified	20. LIMITATION OF ABSTRACT Unlimited	

